Case Studies in Thermal Engineering 27 (2021) 101167

Contents lists available at ScienceDirect

Case Studies in Thermal Engineering

journal homepage: www.elsevier.com/locate/csite

Forced vibration characteristics of embedded graphene oxide powder reinforced metal foam nanocomposite plate in thermal environment

Jie Zheng [a], Chunwei Zhang [a,*], Farayi Musharavati [b,**], Afrasyab Khan [c], Tamer A. Sebaey [d,e], A. Eyvazian [a,f,g]

[a] Structural Vibration Control Group, Qingdao University of Technology, Qingdao, 266033, China
[b] Department of Mechanical and Industrial Engineering, College of Engineering, Qatar University, P.O. Box 2713, Doha, Qatar
[c] Institude of Engineering and Technology, Department of Hydraulics and Hydraulic and Pneumatic Systems, South Ural State University, Lenin Prospect 76, Chelyabinsk, 454080, Russian Federation
[d] Engineering Management Department, College of Engineering, Prince Sultan University, Riyadh, Saudi Arabia
[e] Mechanical Design and Production Department, Faculty of Engineering, Zagazig University, P.O. Box 44519, Zagazig, Sharkia, Egypt
[f] Department of Mechanical Engineering, Politecnico di Milano, 20156, Milan, Italy
[g] Program in Materials Science and Engineering, American University of Sharjah, Sharjah, United Arab Emirates

ARTICLE INFO

Keywords:
Forced vibration
Refined higher order plate theory
Graphene oxide powders
Metal foam
Thermal and dynamic loadings

ABSTRACT

Dynamic behavior of a new class of nanocomposites consisted of metal foam as matrix and graphene oxide powders as reinforcement is presented in this study in the framework of forced vibration. Graphene oxide powders are dispersed through the thickness of a plate made from metal foam material according to four various functionally graded patterns on the basis of the Halpin-Tsai micromechanical homogenization method. Also, three kinds of porosity distributions including two symmetric and one uniform patterns are considered for the metal foam matrix. As external effects, the plate is rested on the Winkler-Pasternak substrate and under uniform thermal and transverse dynamic loadings. By an incorporation of the refined higher order plate theory and Hamilton's principle, the governing equations of the dynamically loaded graphene oxide powder reinforced metal foam nanocomposite plate are derived and then solved with Galerkin exact solution method to achieve the resonance frequencies and dynamic deflections of the structure. Moreover, the influence of different boundary conditions is taken into account. The results indicate that the forced vibrational response of the graphene oxide powder strengthened metal foam nanocomposite plate is dramatically dependent on various parameters such as graphene oxide powders' weight fraction, different boundary conditions, various porosity distributions, foundation parameters and temperature change of uniform thermal loading.

1. Introduction

In recent years, lightweight materials have gained the consideration of many engineering science researchers due to their desirable

* Corresponding author.
** Corresponding author.
E-mail addresses: zhangchunwei@qut.edu.cn (C. Zhang), farayi@qu.edu.qa (F. Musharavati), eyvazian@qu.edu.qa (A. Eyvazian).

https://doi.org/10.1016/j.csite.2021.101167
Received 18 November 2020; Received in revised form 18 April 2021; Accepted 15 June 2021
Available online 19 June 2021

stiffness to weight ratio. Also, metal foam structure, as an extremely lightweight cellular structure comprising of solid metal with gas-filled pores containing the majority of the volume, is an appropriate and lucrative class of lightweight materials employed by several industries such as mechanical, automotive, aerospace, and civil engineering owing to their broad applications provided by eligible attributes suchlike high damping capacity and energy decadence. In addition, dispersing of the porosity or foams continuously along with the thickness or other directions makes us able to adjust the relevant parameters for attaining particular purposes. Therefore, these types of materials became attractive to explore for some researchers.

In order to acquire and detect the mechanical behavior of metal foams, researchers have worked on vibration, bending, and buckling analysis of aforesaid interesting structures. Magnucki and Stasiewicz [1] analytically and by means of finite element method (FEM) investigated the elastic buckling issue of the metal foam beam constructions. Smith et al. [2] studied the metal foams advantages and characteristics such as their raised machinability, adjustable density and porosity. Chen et al. [3] studied the free and also forced dynamic behavior of metal foam beams, in which the porosity distributed in the functionally graded form and also it is explored that symmetric porosity variation is efficient for achieving the largest stiffness in this structure. Furthermore, Chen et al. [3] explored free and also forced vibration demeanor of shear deformable functionally graded dispersed metal foam beams, in the framework of Timoshenko beam theory. Buckling behavior of a circular functionally graded porous plate, in which the pores are saturated with liquid and also porosity is distributed along the thickness direction, is presented by Jabbari et al. [4]. Free vibration of the Levy-type rectangular metal foam plate is explored by Rezaei and Saidi [5] in the Carrera Unified Formulation framework. Wave propagation behavior of porous beams using both Euler–Bernoulli and also Timoshenko beam theories is studied by Wang et al. [6]. Jasion et al. [7] presented the analytical, experimental and numerical investigation of buckling characteristics of sandwich beams and circular plates, in which the core of sandwich structure is a porous material to enhance the stiffness. The vibrational behavior of the FG laminated plate with porous core was investigated by Safaei [8] with utilizing a FEM to show that this porous core can improve the natural frequency responses of laminated composites. Liu et al. [9] investigated the experimental research on dynamic characteristics of porous materials, according to direct impact Hopkinson bar test. Belica et al. [10] conducted the dynamic stability of an isotropic porous cylindrical shell utilizing Galerkin's procedure. Recently, propagation of waves in metal foam plates and shell resting on an elastic substrate was probed by Ebrahimi and Seyfi [11], Ebrahimi and Seyfi [12].

Nowadays, engineers believe that the supreme mechanical characteristics of nano-particles are advantageous enough to be used as reinforcement in composites. Nanocomposite materials including at least one nano-size element utilized as reinforcement for polymeric matrix, play a vital role in modern industries owing to their outstanding characteristics, that, they are unattainable by using single constituents alone. Researchers discovered some enhancements in the stiffness, electrical performance and morphological characteristics of nanocomposite materials behavior. Some of these famous nano-scale reinforcements can be carbon nanotube (CNT), graphene, and graphene platelet (GPL), which are important category of technological reinforcing elements that possesses innumerable lucrative and novel attributes. Nanocomposite structures can be in both macro and nano scales but they are completely different from the structures in micro or nano-scales [13–18]. Accordingly, it is of great significance to investigate the mechanical demeanor of these strengthened composites. The effect of employing of three various types of graphene based reinforcements on fracture toughness and also failure mechanism on nanocomposites is conducted by Chandrasekaran et al. [19]. The effect of CNTs and GPLs on the heat transfer response of polymer nanocomposite cylinders was surveyed by Behdinan et al. [20]. Carbon nanotube-reinforced nanocomposites (CNTRCs) is considered in terms of analyzing vibration behavior employing Eshelby–Mori–Tanaka method by Formica et al. [21]. Static and also free vibration characteristics of CNTRCs plates using diverse methods and considering different frameworks investigated by Alibeigloo and Emtehani [22], Zhu et al. [23]. Bending, buckling and vibration demeanor of CNTRC beams embedded on Winkler-Pasternak foundation, employing higher-order shear deformation theories, explored by Wattanasakulpong and Ungbhakorn [24]. Post-buckling behavior of through thickness functionally graded CNTRC (FG-CNTRC) cylindrical panels resting on elastic substrate employing higher-order shear deformation theory (HSDT) is conducted by Shen and Xiang [25]. An extensive research on vibration characteristics of functionally graded carbon nanotube (FG-CNTRC) implementing FEM, presented by Heshmati et al. [26] to indicate the influence of various parameters such as CNT's waviness or length on nanocomposite materials properties. First-order shear deformation theory (FSDT) and the kp-Ritz approach is utilized to study the free vibration behavior of laminated FG-CNTRC plates by Lei et al. [27]. Laminated CNTRC plates considered in terms of studying the post-buckling behavior by Zhang et al. [28] employing the FSDT. Song et al. [29] implemented the Reddy's theory in order to investigate the dynamic demeanor of diverse distribution types of FG-CNTRC under impact loading. Ansari et al. [30] conducted the vibration and also buckling analysis of through thickness FG-CNTR nanocomposite plates resting on elastic foundation subjected to thermal loading, applying the variational differential quadrature approach. Garcia-Macias et al. [31] explored the agglomeration influence of carbonic FG nanocomposite plates on the bending and also free vibration demeanor, using Mori-Tanaka model. Pourasghar and Chen [32] conducted the thermo-elastic solution of FG-CNTRC cylindrical panels utilizing combined implementation of the differential quadrature method (DQM) and the Newton Raphson approach. Furthermore, single-walled carbon nanotubes (SWCNTs) owing to their great ongoing utilization and benefits such as reinforcements in composite materials, catalysts, additives in polymers, so on and so forth. The Ritz method is employed by Ke et al. [33] to explore the nonlinear vibration demeanor of SWCNTs in which, CNT-reinforcements are supposed to be graded in special direction to achieve some desired characteristics. The axial buckling analysis of the single-layer graphene sheet embedded on two-parameter elastic foundation was conducted by Fattahi et al. [34] on the basis of three different theories. Chatterjee et al. [35] studied the mechanical behavior of epoxy matrix reinforced with graphene nanoplatelets (GNPs) and also diverse mixture ratios of CNTs beside GNPs. Yadav and Cho [36] explored the consequence of the functionalized GNPs on mechanical and also thermal characteristics of GPL-reinforced nanocomposites by Raman spectroscopy technique. Yang et al. [37] explored buckling and also postbuckling behavior of multi-layered nanocomposite beams strengthened with GPLs through FSDT. Song et al. [38] applied FSDT to study both free and forced vibration characteristics of GPL-strengthened composite plates. Feng et al. [39]

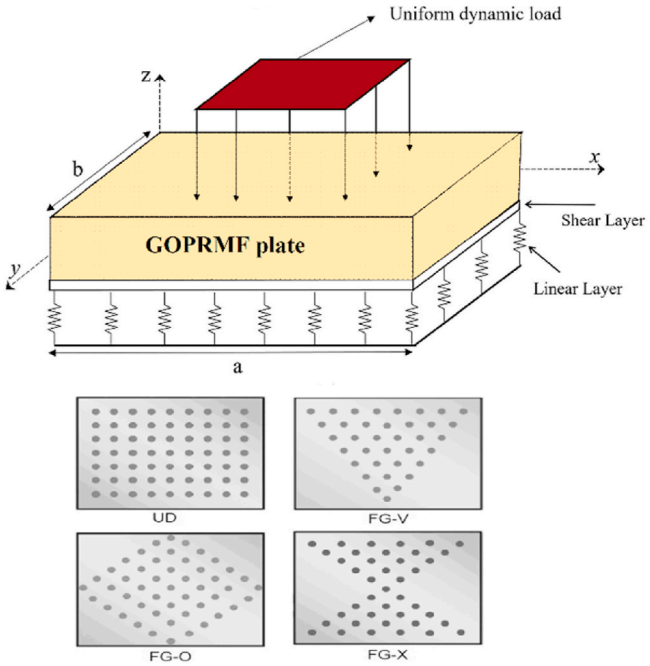

Fig. 1. Schematic diagram for geometry of the plate and four various types of GOP distributions.

investigated the nonlinear vibration demeanor of a multi-layered through thickness dispersed GPL-reinforced nanocomposite beams by means of Ritz method. Natural frequency analysis of GPL-reinforced nanocomposite beams embedded on viscoelastic substrate using Navier's solution method is studied by Qaderi et al. [40]. Liu et al. [41] conducted both buckling and also free vibration behavior of multi-layered nonlinearly through thickness dispersed GPL-reinforced nanocomposite cylindrical shells within the framework of three-dimensional elasticity theory. Analytical solutions for bending and buckling characteristics of nanocomposite plates reinforced with functionally graded GPLs implementing FSDT explored by Song et al. [42]. Afterward, Shen et al. [43] investigated the nonlinear bending demeanor of laminated FG graphene reinforced nanocomposite panels rested on elastic substrate by means of Reddy's theory. Also, some researchers have studied the wave dispersion behavior of GPL or CNT (carbon-based reinforcements) reinforced nanocomposites subjected to various conditions and effects [44–48]. Besides, some researchers [49,50] have applied porosity patterns in CNT or GPL reinforced nanocomposite structures to investigate how this effect can influence the mechanical responses of these nanocomposites.

Furthermore, there is one more type of carbonic nanoparticle, known as graphene oxide, that represented adequate astounding characteristics to be utilized as reinforcement in composite materials, for instance, its desirable mechanical performance with low cost and also it is more compatible in association with polymers [51–55]. GO is an intensely-oxidized form of graphene itself and has sufficient oxygen-containing groups within it. In addition to all applications of GO such as energy and power industry, biomedical procedures, super-capacitor material, batteries, LED technologies, graphene oxide powders (GOPs) is a novel nano-scale reinforcement especially for polymer nanocomposites [56]. Accordingly, these materials have attracted the researcher's interest. Experimental studies on elastic parameters of single layer GO by Gómez-Navarro et al. [57] indicated the Young's modulus about 0.25 ± 0.25 TPa. It is investigated by Tang et al. [58] that, various types of dispersion model of graphene oxides (GOs) have different results on mechanical and thermal behavior of graphene/epoxy composites, that this effects found and studied in this article. Zhang et al. [59] explored the bending, buckling, and also natural frequency characteristics of functionally graded GOPs reinforced multi-layered composite beams by means of FSDT, and it is indicated that using GOP is more effective to enhance the mechanical properties of matrix, compared with other carbonic reinforcements. Moreover, vibration behavior of functionally graded GOP-reinforced nanocomposite plates subjected to various thermal behaviors and rested elastic and viscoelastic foundations is studied by Ebrahimi et al. [60,61]. Likewise, Ebrahimi et al. [62] surveyed the vibration demeanor of GOP reinforced nanocomposite beams under a non-uniform magnetic field utilizing Galerkin's method. Buckling characteristics of GOP reinforced nanocomposite structures subjected to thermal loading or magnetic fields investigated by Ebrahimi et al. [63,64]. Wave propagation behavior of GOP reinforced nanocomposite plates under various thermal situations by means of refined higher order plate theory is conducted by Ebrahimi et al. [56]. According to the best of the authors' knowledge, from the literature survey, it may be discovered that forced dynamic analysis of graphene oxide powder strengthened metal foam (GOPRMF) nanocomposite plate subjected to thermal environment is a novel subject which is not conducted hitherto.

In this paper, the forced vibration and resonance behaviors of the metal foam plate reinforced with GOPs are studied for the first time. As mentioned above, GOPs have astounding properties which make them to be considered as a novel nano reinforcement. Also, an advanced theory with the name of "Refined Higher Order Plate Theory" have been utilized in which there is no need to use shear

Table 1
The mechanical properties of the constitutive materials for the GOPRMF nanocomposite plate.

Metal matrix (ASTM A36 steel)	Reinforcement phase (GOP)
$E_m = 200Gpa$	$E_{GOP} = 444.8\ GPa$
$\nu_m = 0.26$	$\nu_{GOP} = 0.165$
$\rho_m = 7850\ kg/m^3$	$\rho_{GOP} = 1090\ kg/m^3$
$G_m = 79.3Gpa$	$G_{GOP} = 190.9Gpa$
$\alpha_m = 1.2\times 10^{-5}\ 1/K$	$\alpha_{GOP} = -5\times 10^{-5}\ 1/K$

correction factor and also it is as simple as classical theories in many aspects but with very more accurate responses due to considering shear deformations. Besides, the influence of some other parameters such as thermal loading and elastic foundation on the resonance response of this structure are investigated. The new results of this paper indicate that adding GOPs to the metal foam plate will significantly improve the stiffness of the structure which can postpone the resonance phenomena and decrease the deflection of the metal foam plate.

2. Theoretical formulations and mathematical relations

2.1. Micromechanical material homogenization

2.1.1. Effective material properties of the GOP reinforced metal plate

The under-study structure shown in Fig. 1, includes steel material used as matrix, which the material properties brought in Table 1, and the GOPs distributed as reinforcement of the metal matrix. In addition, it is observable that the structure is embedded on a foundation consisted of Winkler and Pasternak layers. Also, it is indicated in the aforementioned figure, the reinforcement powders dispersed according to different patterns, such as UD (uniform distribution), FG-X, FG-O and FG-V functions. These patterns may be induced via putting the nano-powders in a series of determined circumstances, which can be computed by following formulations:

$$\begin{cases} V_{GOP} = V_{GOP}^{T} & \text{GOPR (UD)} \\ V_{GOP} = \left(2 - 4\dfrac{|z|}{h}\right)\times V_{GOP}^{T} & \text{GOPR (FG}-\text{O)} \\ V_{GOP} = 4\dfrac{|z|}{h}\times V_{GOP}^{T} & \text{GOPR (FG}-\text{X)} \\ V_{GOP} = \left(1 + 2\dfrac{z}{h}\right)\times V_{GOP}^{T} & \text{GOPR (FG}-\text{V)} \end{cases} \tag{1}$$

where, h indicates the thickness of plate and also V_{GOP}^{T} represents the reinforcements' total volume fraction the can be stated as:

$$V_{GOP}^{T} = \frac{1}{1 + \left(\frac{\rho_{GOP}}{\rho_{M}}\right)\left(\frac{1}{W_{GOP}} - 1\right)} \tag{2}$$

in which, the subscripts M and GOP belong to the matrix material (steel) and the GOP reinforcements, respectively. Moreover, W and ρ stand for the weight fraction and mass density, respectively. The next step is to obtain the effective values of required parameters such as Young's modulus, poison's ratio and coefficient of thermal expansion (CTE) of reinforced nanocomposite. In this study, the derivation of the material characteristics developed by means of Halpin-Tsai homogenization approach [59,65]. Eventually, the Young's modulus may be derived as follows:

$$E_{GOPR} = 0.49E_l + 0.51E_t \tag{3}$$

where, E_l and E_t represents the longitudinal and transverse Young's modulus of the GOP reinforced nanocomposite, respectively. These aforementioned values can be calculated according to Zhang et al. [59]:

$$E_l = \frac{E_M \times (1 + \xi_l\, \eta_l\, V_{GOP})}{1 - \eta_l\, V_{GOP}}, \quad E_t = \frac{E_M \times (1 + \xi_t\, \eta_t\, V_{GOP})}{1 - \eta_t\, V_{GOP}} \tag{4}$$

in which

$$\eta_l = \frac{\left(\frac{E_{GOP}}{E_M}\right) - 1}{\left(\frac{E_{GOP}}{E_M}\right) + \xi_l}, \quad \eta_t = \frac{\left(\frac{E_{GOP}}{E_M}\right) - 1}{\left(\frac{E_{GOP}}{E_M}\right) + \xi_t} \tag{5}$$

where, E belongs to Young's modulus parameter and also, the geometry factors (ξ_l and ξ_t) can be calculated as below Zhang et al. [59]:

$$\xi_l = \xi_t = \frac{2d_{GOP}}{h_{GOP}} \tag{6}$$

in which d_{GOP} and h_{GOP} correspond with GOPs' diameter and thickness, respectively. Afterward, the rule of mixture is implemented to derive the effective Poisson's ratio of the reinforced nanocomposite, as it is mentioned below:

$$\nu_{GOPR} = \nu_M V_M + \nu_{GOP} V_{GOP} \tag{7a}$$

$$\rho_{GOPR} = \rho_M V_M + \rho_{GOP} V_{GOP} \tag{7b}$$

where, V and ν stand for volume fraction and Poisson's ratio of subscript of each term, respectively. It must be stated that the effective mass density may be calculated in the same way as Poisson's ratio is obtained in Eq. (7). The following relation can be indicated how the volume fractions are related to each other:

$$V_{GOP} + V_M = 1 \tag{8}$$

thereafter, coefficient of thermal expansion (CTE) have to be achieved for GOP reinforced nanocomposites using the below equation Van Es [65]:

$$\alpha_{GOPR} = \alpha_M + \frac{(\alpha_M + \alpha_{GOP})\left(\frac{1}{K_{eff}} + \frac{1}{K_M}\right)}{\frac{1}{K_M} + \frac{1}{K_{GOP}}} \tag{9}$$

where K denotes the bulk moduli and α represents the CTE that each parameter belongs to the subscript materials.

2.1.2. *Various porosity dispersion model of the metal foam plate reinforced with GOPs*

The considered metal matrix GOP is assumed to be made of a metal foam material. Further, three types of porosity distribution supposed to be taken into account. All the porosity types presumed to be symmetric with respect to mid-plane. Then, in porosity distribution symmetric type I the size of pores decreases from mid-plane to the outer surfaces (the mid-plane contains the largest size of pores) and also in porosity distribution symmetric type II the size of pores decreases from outer surfaces to the mid-plane (the mid-plane contains the smallest size of pores). Evidently, these two types of pore dispersions display graded features similar to FG materials [66–73]. The other type of distribution contains the pores with the same size all over the thickness.

$$E(z) = \begin{cases} E_{GOPR}\left(1 - e_1 \cos\left(\frac{\pi z}{h}\right)\right) & \text{Porosity distribution 1} \\ E_{GOPR}\left[1 - e_2\left(1 - \cos\left(\frac{\pi z}{h}\right)\right)\right] & \text{Porosity distribution 2} \\ E_{GOPR} \times e_3 & \text{Uniform porosity distribution} \end{cases} \tag{10}$$

$$\rho(z) = \begin{cases} \rho_{GOPR}\left(1 - e_{m1} \cos\left(\frac{\pi z}{h}\right)\right) & \text{Porosity distribution 1} \\ \rho_{GOPR}\left[1 - e_{m2}\left(1 - \cos\left(\frac{\pi z}{h}\right)\right)\right] & \text{Porosity distribution 2} \\ \rho_{GOPR} \times e_{m3} & \text{Uniform porosity distribution} \end{cases} \tag{11}$$

$$\mu(z) = \mu_{GOPR} \tag{12}$$

The relation between Young's modulus E(z) and mass density ρ(z) is expressed using the Young's modulus and mass density of GOP reinforced nanocomposite (E_{GOPR} *and* ρ_{GOPR}), as below [74–76]:

$$\frac{\rho(z)}{\rho_{GOPR}} = \left(\frac{E(z)}{E_{GOPR}}\right)^{1/2} \tag{13}$$

The mass density (e_{m1},e_{m2}, and e_{m3}) and porosity coefficients (e_1, e_2, and e_3) are formulated as below Yang et al. [76]:

$$\begin{cases} \left(1-e_1\cos\left(\frac{\pi z}{h}\right)\right)=\left(1-e_{m1}\cos\left(\frac{\pi z}{h}\right)\right)^2 \\ \left[1-e_2\left(1-\cos\left(\frac{\pi z}{h}\right)\right)\right]=\left[1-e_{m2}\left(1-\cos\left(\frac{\pi z}{h}\right)\right)\right]^2 \\ e_3=(e_{m3})^2 \end{cases} \tag{14}$$

According to the premise that the entire mass of GOP reinforced nanocomposite metal foam plates with different porosity or GOP dispersion are equivalent, we have:

$$\int_0^{h/2}\left(1-e_1\cos\left(\frac{\pi z}{h}\right)\right)^{1/2}dz=\int_0^{h/2}\left(1-e_2\cos\left(\frac{\pi z}{h}\right)\right)^{1/2}dz=\int_0^{h/2}(e_3)^{1/2}dz \tag{15}$$

2.2. Refined higher-order shear deformable plate theory

This section is allocated to the kinematic formulization of aforementioned plate element to obtain a set of preliminary equations, in order to employ them to achieve the governing equations of a plate. The displacement-based theories can be divided into the classical plate theory and shear deformation plate theories. The classical plate theory (CPT) neglected transverse shear strains and assumed that normal to the mid-plane before deformation remain straight and normal to the plane after deformation. Thus, the classical theory can be only used for thin plates and will give erroneous results when being used for thick plates, especially the plates made of advanced composites Thereupon, the refined higher-order shear deformable plate theory developed via researchers, in order to assess the shear stress and strain of the plate. In this regard, a shape function is stated in each theory. Herein, the refined shape of sinusoidal plate theory is implemented for the sake of achieving the kinematic relations of the plate. The most interesting feature of this theory is that it does not require shear correction factor, and has strong similarities with the CPT in some aspects such as governing equation, boundary conditions and moment expressions. Based on this theory, the plate's displacement fields can be formulated as below Belkorissat et al. [77]:

$$u_x(x,y,z)=u(x,y)-z\frac{\partial w_b}{\partial x}-f(z)\frac{\partial w_s}{\partial x} \tag{16}$$

$$u_y(x,y,z)=v(x,y)-z\frac{\partial w_b}{\partial y}-f(z)\frac{\partial w_s}{\partial y} \tag{17}$$

$$u_z(x,y,z)=w_b(x,y)+w_s(x,y) \tag{18}$$

in which, u, v, w_b and w_s stand for longitudinal and transverse displacements, bending and shear deflections, respectively. The associated shape functions of the implemented theory can be written as follows Ebrahimi et al. [61]:

$$f(z)=z-\frac{h}{\pi}\sin\left(\frac{\pi z}{h}\right) \tag{19}$$

Also, the nonzero strains of the plate can be stated as the following equations:

$$\begin{aligned} &\begin{Bmatrix}\varepsilon_x\\ \varepsilon_y\\ \gamma_{xy}\end{Bmatrix}=\begin{Bmatrix}\varepsilon_x^0\\ \varepsilon_y^0\\ \gamma_{xy}^0\end{Bmatrix}+z\begin{Bmatrix}k_x^b\\ k_y^b\\ k_{xy}^b\end{Bmatrix}+f(z)\begin{Bmatrix}k_x^s\\ k_y^s\\ k_{xy}^s\end{Bmatrix}, \\ &\begin{Bmatrix}\gamma_{yz}\\ \gamma_{xz}\end{Bmatrix}=g(z)\left(\begin{Bmatrix}\gamma_{yz}^s\\ \gamma_{xz}^s\end{Bmatrix}+\begin{Bmatrix}\gamma_{yz}^b\\ \gamma_{xz}^b\end{Bmatrix}\right) \end{aligned} \tag{20}$$

in which,

$$\left\{\begin{array}{c}\varepsilon_x^0\\ \varepsilon_y^0\\ \gamma_{xy}^0\end{array}\right\}=\left\{\begin{array}{c}\dfrac{\partial u}{\partial x}\\ \dfrac{\partial v}{\partial y}\\ \dfrac{\partial u}{\partial y}+\dfrac{\partial v}{\partial x}\end{array}\right\},\quad \left\{\begin{array}{c}k_x^b\\ k_y^b\\ k_{xy}^b\end{array}\right\}=\left\{\begin{array}{c}-\dfrac{\partial^2 w_b}{\partial x^2}\\ -\dfrac{\partial^2 w_b}{\partial y^2}\\ -2\dfrac{\partial^2 w_b}{\partial x\partial y}\end{array}\right\},\quad \left\{\begin{array}{c}k_x^s\\ k_y^s\\ k_{xy}^s\end{array}\right\}=\left\{\begin{array}{c}-\dfrac{\partial^2 w_s}{\partial x^2}\\ -\dfrac{\partial^2 w_s}{\partial y^2}\\ -2\dfrac{\partial^2 w_s}{\partial x\partial y}\end{array}\right\} \tag{21}$$

$$\left\{\begin{array}{c}\gamma_{yz}^s\\ \gamma_{xz}^s\end{array}\right\}=\left\{\begin{array}{c}\dfrac{\partial w_s}{\partial y}\\ \dfrac{\partial w_s}{\partial x}\end{array}\right\},\quad \left\{\begin{array}{c}\gamma_{yz}^b\\ \gamma_{xz}^b\end{array}\right\}=\left\{\begin{array}{c}\dfrac{\partial w_b}{\partial y}\\ \dfrac{\partial w_b}{\partial x}\end{array}\right\},\qquad g(z)=1-\frac{df(z)}{dz}$$

2.3. Hamilton's principle

Herein, Hamilton's principle which is utilized to obtain the Euler-Lagrange equation, is expressed as follows:

$$\int_0^t \delta(U+\Pi+T)\,dt=0 \tag{22}$$

where, U belongs to the strain energy, Π belongs to the work done by external forces and T belongs to the kinetic energy, respectively. The strain energy's variation is expressed as below:

$$\delta U=\int_V \sigma_{ij}\delta\varepsilon_{ij}dV=\int_V\left(\sigma_x\delta\varepsilon_x+\sigma_y\delta\varepsilon_y+\sigma_{xy}\delta\gamma_{xy}+\sigma_{yz}\delta\gamma_{yz}+\sigma_{xz}\delta\gamma_{xz}\right)dV \tag{23}$$

Substituting equations. (16)–(21) in Eq. (23) yields:

$$\delta U=\int_0^L\left(\begin{array}{l}N_x\dfrac{\partial\delta u}{\partial x}-M_x^b\dfrac{\partial^2\delta w_b}{\partial x^2}-M_x^s\dfrac{\partial^2\delta w_s}{\partial x^2}+Q\dfrac{\partial w_s}{\partial x}+N_y\dfrac{\partial\delta v}{\partial y}\\ -M_y^b\dfrac{\partial^2\delta w_b}{\partial y^2}-M_y^s\dfrac{\partial^2\delta w_s}{\partial y^2}+N_{xy}\left(\dfrac{\partial\delta u}{\partial y}+\dfrac{\partial\delta v}{\partial x}\right)\\ -2M_{xy}^b\dfrac{\partial^2\delta w_b}{\partial x\partial y}-2M_{xy}^s\dfrac{\partial^2\delta w_s}{\partial x\partial y}+Q_{yz}\dfrac{\partial\delta w_s}{\partial y}+Q_{xz}\dfrac{\partial\delta w_s}{\partial x}\end{array}\right)dx \tag{24}$$

where the utilized parameters introduced at the last equation are expressed as follows:

$$\left[N_i\quad M_i^b\quad M_i^b\right]=\int_A\left[1\quad z\quad f(z)\right]\sigma_i\,dA,\qquad \mathrm{i}=(\mathrm{x},\ \mathrm{y},\ \mathrm{xy}) \tag{25}$$

$$Q_i=\int_A g(z)\,\sigma_i\,dA,\qquad \mathrm{i}=(\mathrm{xz},\ \mathrm{yz}) \tag{26}$$

then, the first variation of work done by applied forces (Π) can be written as below:

$$\delta\Pi=\int_0^L\left(\begin{array}{l}\left(N_x^T\right)\dfrac{\partial\delta(w_b+w_s)}{\partial x}\dfrac{\partial(w_b+w_s)}{\partial x}-\left(k_w-q_{dynamic}\right)\delta(w_b+w_s)+k_p\\ +\dfrac{\partial^2\delta(w_b+w_s)}{\partial x^2}+\left(N_y^T\right)\dfrac{\partial\delta(w_b+w_s)}{\partial y}\dfrac{\partial(w_b+w_s)}{\partial y}\\ +2\delta N_{xy}^0\dfrac{\partial(w_b+w_s)}{\partial x}\dfrac{\partial(w_b+w_s)}{\partial y}\end{array}\right)dx \tag{27}$$

k_w and k_p presented in the above equation are belong to Winkler and Pasternak substrates coefficients [78], respectively. Also, $q_{dynamic}$ is the transverse dynamic loading. In addition, it is considered that a biaxial thermal loading ($N_x^T=N_y^T=N^T$) is applied to the under-study plate structure; besides, the shear loading is ignored ($N_{xy}^0=0$). Hence, the thermal loading (N^T) can be expressed as [79]:

Table 2
The acceptable functions $X_m(x)$ and $Y_n(y)$ for various B.Cs [80].

Edge condition	The functions $X_m(x)$ and $Y_n(y)$		B.Cs	
	$X_m(x)$	$Y_n(y)$	At $x = 0, a$	At $y = 0, b$
S–S–S–S	$\sin(\alpha x)$	$\sin(\beta y)$	$X_m(0) = X_m^{'}(0) = 0$	$Y_n(0) = Y_n^{'}(0) = 0$
			$X_m(a) = X_m^{'}(a) = 0$	$Y_n(b) = Y_n^{'}(b) = 0$
C–C–S–S	$sin^2(\alpha y)$	$\sin(\beta y)$	$X_m(0) = X_m^{'}(0) = 0$	$Y_n(0) = Y_n^{'}(0) = 0$
			$X_m(a) = X_m^{'}(a) = 0$	$Y_n(b) = Y_n^{'}(b) = 0$
C–C–C–C	$sin^2(\alpha y)$	$sin^2(\beta y)$	$X_m(0) = X_m^{'}(0) = 0$	$Y_n(0) = Y_n^{'}(0) = 0$
			$X_m(a) = X_m^{'}(a) = 0$	$Y_n(b) = Y_n^{'}(b) = 0$

$$N^T = \int_{-h/2}^{h/2} \left(\frac{E_{GOPR}}{1 - \nu_{GOPR}} \alpha_{GOPR} \Delta T \right) dz \tag{28}$$

moreover, the conversion of the kinetic energy can be defined as:

$$\delta T = \int_0^a \int_0^b \left(\begin{array}{l} I_0 \left(\frac{\partial u}{\partial t} \frac{\partial \delta u}{\partial t} + \frac{\partial v}{\partial t} \frac{\partial \delta v}{\partial t} + \frac{\partial (w_b + w_s)}{\partial t} \frac{\partial \delta (w_b + w_s)}{\partial t} \right) \\ -I_1 \left(\frac{\partial u}{\partial t} \frac{\partial \delta w_b}{\partial x \partial t} + \frac{\partial w_b}{\partial x \partial t} \frac{\partial \delta u}{\partial t} + \frac{\partial v}{\partial t} \frac{\partial \delta w_b}{\partial y \partial t} + \frac{\partial w_b}{\partial y \partial t} \frac{\partial \delta v}{\partial t} \right) \\ +I_2 \left(\frac{\partial w_b}{\partial x \partial t} \frac{\partial \delta w_b}{\partial x \partial t} + \frac{\partial w_b}{\partial y \partial t} \frac{\partial \delta w_b}{\partial y \partial t} \right) \\ -J_1 \left(\frac{\partial u}{\partial t} \frac{\partial \delta w_s}{\partial x \partial t} + \frac{\partial w_b}{\partial x \partial t} \frac{\partial \delta u}{\partial t} + \frac{\partial v}{\partial t} \frac{\partial \delta w_s}{\partial y \partial t} + \frac{\partial w_s}{\partial y \partial t} \frac{\partial \delta v}{\partial t} \right) \\ +K_2 \left(\frac{\partial w_s}{\partial x \partial t} \frac{\partial \delta w_s}{\partial x \partial t} + \frac{\partial w_s}{\partial y \partial t} \frac{\partial \delta w_s}{\partial y \partial t} \right) \\ +J_2 \left(\frac{\partial w_b}{\partial x \partial t} \frac{\partial \delta w_s}{\partial x \partial t} + \frac{\partial w_s}{\partial x \partial t} \frac{\partial \delta w_b}{\partial x \partial t} + \frac{\partial w_b}{\partial y \partial t} \frac{\partial \delta w_s}{\partial y \partial t} + \frac{\partial w_s}{\partial y \partial t} \frac{\partial \delta w_b}{\partial y \partial t} \right) \end{array} \right) dxdy \tag{29}$$

in which

$$[\, I_0 \quad I_1 \quad J_1 \quad I_2 \quad J_2 \quad K_2 \,] = \int_{-h/2}^{h/2} [\, 1 \quad z \quad f \quad z^2 \quad zf(z) \quad f^2(z) \,] \rho(z) dz \tag{30}$$

hereon, by replacing Eqs. (24), (27) and (29) into Eq. (22) and setting the coefficients of δu, δv, δw_b and δw_s equal to zero, the below Euler–Lagrange equation may be achieved:

$$\frac{\partial N_x}{\partial x}+\frac{\partial N_{xy}}{\partial y}=I_0\frac{\partial^2 u}{\partial t^2}-I_1\frac{\partial^3 w_b}{\partial x\partial t^2}-J_1\frac{\partial^3 w_s}{\partial x\partial t^2} \tag{31}$$

$$\frac{\partial N_{xy}}{\partial x}+\frac{\partial N_y}{\partial y}=I_0\frac{\partial^2 v}{\partial t^2}-I_1\frac{\partial^3 w_b}{\partial y\partial t^2}-J_1\frac{\partial^3 w_s}{\partial y\partial t^2} \tag{32}$$

$$\begin{aligned}&\frac{\partial^2 M_x^b}{\partial x^2}+2\frac{\partial^2 M_{xy}^b}{\partial x\partial y}+\frac{\partial^2 M_y^b}{\partial y^2}+\frac{\partial Q}{\partial x}-N^T\nabla^2(w_b+w_s)\\ &-k_w(w_b+w_s)+k_p\nabla^2(w_b+w_s)=q_{dynamic}+I_0\frac{\partial^2(w_b+w_s)}{\partial t^2}+I_1\left(\frac{\partial^3 u}{\partial x\partial t^2}+\frac{\partial^3 v}{\partial y\partial t^2}\right)\\ &-I_2\nabla^2\left(\frac{\partial^2 w_b}{\partial t^2}\right)-J_2\nabla^2\left(\frac{\partial^2 w_s}{\partial t^2}\right)\end{aligned} \tag{33}$$

$$\begin{aligned}&\frac{\partial^2 M_x^s}{\partial x^2}+2\frac{\partial^2 M_{xy}^s}{\partial x\partial y}+\frac{\partial^2 M_y^s}{\partial y^2}+\frac{\partial Q_{xy}}{\partial x}+\frac{\partial Q_{yz}}{\partial y}-N^T\nabla^2(w_b+w_s)\\ &-k_w(w_b+w_s)-k_p\nabla^2(w_b+w_s)=q_{dynamic}+I_0\frac{\partial^2(w_b+w_s)}{\partial t^2}+J_1\left(\frac{\partial^3 u}{\partial x\partial t^2}+\frac{\partial^3 v}{\partial y\partial t^2}\right)\\ &-J_2\nabla^2\left(\frac{\partial^2 w_b}{\partial t^2}\right)-K_2\nabla^2\left(\frac{\partial^2 w_s}{\partial t^2}\right)\end{aligned} \tag{34}$$

where ∇^2 belong to the Laplacian operator.

2.4. Constitutive equations

In this section, the stresses and strains of the proposed structure will be related to each other via following general constitutive equations:

$$\sigma_{ij}=T_{ijkl}\varepsilon_{kl} \tag{35}$$

in which, σ_{ij} is the second order stress tensor and also ε_{kl} is the second order strain tensor. Whilst, T_{ijkl} is associated with the components of the fourth order elasticity tensor. While, expanding the above equations for an element containing shear strains, below expressions will be derived:

$$\begin{bmatrix}\sigma_{xx}\\ \sigma_{yy}\\ \sigma_{yz}\\ \sigma_{xz}\\ \sigma_{xy}\end{bmatrix}=\begin{bmatrix}Q_{11}&Q_{12}&0&0&0\\ Q_{12}&Q_{22}&0&0&0\\ 0&0&Q_{44}&0&0\\ 0&0&0&Q_{55}&0\\ 0&0&0&0&Q_{66}\end{bmatrix}\left(\begin{bmatrix}\varepsilon_{xx}\\ \varepsilon_{yy}\\ \varepsilon_{yz}\\ \varepsilon_{xz}\\ \varepsilon_{xy}\end{bmatrix}-\begin{bmatrix}\alpha_{11}\\ \alpha_{22}\\ 0\\ 0\\ 0\end{bmatrix}\Delta T\right) \tag{36}$$

in which

$$\begin{aligned}&Q_{11}=\frac{E_{GOPR}}{1-\nu_{GOPR}{}^2}\ ,\quad Q_{12}=\nu_{GOPR}Q_{11}\ ,\quad Q_{22}=Q_{11}\ ,\\ &Q_{44}=Q_{55}=Q_{66}=G_{GOPR}\end{aligned} \tag{37}$$

where E_{GOPR} and G_{GOPR} stand for the Young's and shear moduli of the GOPR nanocomposite, respectively. In addition, integrating from Equations. (31)- (34) over the cross-section area of the plate, the stress resultants equations can be defined as below:

$$\begin{Bmatrix} N_X \\ N_y \\ N_{Xy} \end{Bmatrix} = \begin{pmatrix} A_{11}\ A_{12}\ 0 A_{21}\ A_{22}\ 00\ 0\ A_{66} \end{pmatrix} \begin{Bmatrix} \dfrac{\partial u}{\partial x}\ \dfrac{\partial v}{\partial y}\ \dfrac{\partial u}{\partial y}+\dfrac{\partial v}{\partial x} \end{Bmatrix} + \begin{pmatrix} B_{11}\ B_{12}\ 0 B_{21}\ B_{22}\ 00\ 0\ B_{66} \end{pmatrix} \begin{Bmatrix} -\dfrac{\partial^2 w_b}{\partial x^2} -\dfrac{\partial^2 w_b}{\partial y^2} -2\dfrac{\partial^2 w_b}{\partial x \partial y} \end{Bmatrix} + \begin{pmatrix} B_{11}^s\ B_{12}^s\ 0 B_{21}^s\ B_{22}^s\ 00\ 0\ B_{66}^s \end{pmatrix} \begin{Bmatrix} -\dfrac{\partial^2 w_s}{\partial x^2} -\dfrac{\partial^2 w_s}{\partial y^2} -2\dfrac{\partial^2 w_s}{\partial x \partial y} \end{Bmatrix} \tag{38}$$

$$\begin{Bmatrix} M_x^b \\ M_y^b \\ M_{xy}^b \end{Bmatrix} = \begin{pmatrix} B_{11}\ B_{12} 0 B_{21}\ B_{22}\ 00\ 0\ B_{66} \end{pmatrix} \begin{Bmatrix} \dfrac{\partial u}{\partial x}\ \dfrac{\partial v}{\partial y}\ \dfrac{\partial u}{\partial y}+\dfrac{\partial v}{\partial x} \end{Bmatrix} + \begin{pmatrix} D_{11}\ D_{12}\ 0 D_{21}\ D_{22}\ 00\ 0\ D_{66} \end{pmatrix} \begin{Bmatrix} -\dfrac{\partial^2 w_b}{\partial x^2} -\dfrac{\partial^2 w_b}{\partial y^2} -2\dfrac{\partial^2 w_b}{\partial x \partial y} \end{Bmatrix} + \begin{pmatrix} D_{11}^s\ D_{12}^s\ 0 D_{21}^s\ D_{22}^s\ 00\ 0\ D_{66}^s \end{pmatrix} \begin{Bmatrix} -\dfrac{\partial^2 w_s}{\partial x^2} -\dfrac{\partial^2 w_s}{\partial y^2} -2\dfrac{\partial^2 w_s}{\partial x \partial y} \end{Bmatrix} \tag{39}$$

$$\begin{Bmatrix} M_x^s \\ M_y^s \\ M_{xy}^s \end{Bmatrix} = \begin{pmatrix} B_{11}^s\ B_{12}^s\ 0 B_{21}^s\ B_{22}^s\ 00\ 0\ B_{66}^s \end{pmatrix} \begin{Bmatrix} \dfrac{\partial u}{\partial x}\ \dfrac{\partial v}{\partial y}\ \dfrac{\partial u}{\partial y}+\dfrac{\partial v}{\partial x} \end{Bmatrix} + \begin{pmatrix} D_{11}^s\ D_{12}^s\ 0 D_{21}^s\ D_{22}^s\ 00\ 0\ D_{66}^s \end{pmatrix} \begin{Bmatrix} -\dfrac{\partial^2 w_b}{\partial x^2} -\dfrac{\partial^2 w_b}{\partial y^2} -2\dfrac{\partial^2 w_b}{\partial x \partial y} \end{Bmatrix} + \begin{pmatrix} H_{11}^s\ H_{12}^s\ 0 H_{21}^s\ H_{22}^s\ 00\ 0\ H_{66}^s \end{pmatrix} \begin{Bmatrix} -\dfrac{\partial^2 w_s}{\partial x^2} -\dfrac{\partial^2 w_s}{\partial y^2} -2\dfrac{\partial^2 w_s}{\partial x \partial y} \end{Bmatrix} \tag{40}$$

$$\begin{Bmatrix} Q_x \\ Q_y \end{Bmatrix} = \begin{pmatrix} A^s_{44} & 0 \\ 0 & A^s_{55} \end{pmatrix} \begin{Bmatrix} \dfrac{\partial w_s}{\partial y} \\ \dfrac{\partial w_s}{\partial x} \end{Bmatrix} \tag{41}$$

where in Eq. (38)– (41) the cross-sectional rigidities are represented by the below expressions:

$$\begin{bmatrix} A_{11} & B_{11} & D_{11} & B^s_{11} & D^s_{11} & H^s_{11} \\ A_{12} & B_{12} & D_{12} & B^s_{12} & D^s_{12} & H^s_{12} \\ A_{66} & B_{66} & D_{66} & B^s_{66} & D^s_{66} & H^s_{66} \end{bmatrix} = \int_{-h/2}^{h/2} Q_{11} \begin{bmatrix} 1 \\ \nu_{GOPR} \\ \dfrac{(1-\nu_{GOPR})}{2} \end{bmatrix} \begin{bmatrix} 1 & z & z^2 & f(z) & zf(z) & f^2(z) \end{bmatrix} dz \tag{42}$$

$$\begin{bmatrix} A_{22} & B_{22} & D_{22} & B^s_{22} & D^s_{22} & H^s_{22} \end{bmatrix} = \begin{bmatrix} A_{11} & B_{11} & D_{11} & B^s_{11} & D^s_{11} & H^s_{11} \end{bmatrix} \tag{43}$$

$$A^s_{44} = A^s_{55} = \int_{-h/2}^{h/2} G_{GOPR} g^2(z)\, dz \tag{44}$$

By substituting Equations (38)–(41) into Equations (31)–(34), the governing equations of considered GOPR nanocomposite plate will be defined in terms of displacements (u, v, w_b, and w_s) as:

$$\begin{cases} A_{11}\dfrac{\partial^2 u}{\partial x^2} + (A_{12}+A_{66})\dfrac{\partial^2 v}{\partial x \partial y} + A_{66}\dfrac{\partial^2 u}{\partial y^2} - B_{11}\dfrac{\partial^3 w_b}{\partial x^3} - (B_{12}+2B_{66})\dfrac{\partial^3 w_b}{\partial x \partial y^2} \\ -B^{11}_s\dfrac{\partial^3 w_s}{\partial x^3} - \left(B^s_{12}+2B^s_{66}\right)\dfrac{\partial^3 w_s}{\partial x \partial y^2} - I_0\dfrac{\partial^2 u}{\partial t^2} + I_1\dfrac{\partial^2 w_b}{\partial x \partial t^2} + J_1\dfrac{\partial^2 w_s}{\partial x \partial t^2} = 0 \end{cases} \tag{45}$$

$$\begin{cases} A_{22}\dfrac{\partial^2 v}{\partial y^2} + (A_{12}+A_{66})\dfrac{\partial^2 u}{\partial x \partial y} + A_{66}\dfrac{\partial^2 v}{\partial x^2} - B_{11}\dfrac{\partial^3 w_b}{\partial x^3} - B_{22}\dfrac{\partial^3 w_b}{\partial y^3} - (B_{12}+2B_{66})\dfrac{\partial^2 w_b}{\partial x^2 \partial y} \\ -B^{22}_s\dfrac{\partial^3 w_s}{\partial y^3} - \left(B^s_{12}+2B^s_{66}\right)\dfrac{\partial^3 w_s}{\partial x^2 \partial y} - I_0\dfrac{\partial^2 v}{\partial t^2} + I_1\dfrac{\partial^2 w_b}{\partial y \partial t^2} + J_1\dfrac{\partial^2 w_s}{\partial y \partial t^2} = 0 \end{cases} \tag{46}$$

$$\begin{cases} B_{11}\dfrac{\partial^3 u}{\partial x^3} + (B_{12}+2B_{66})\dfrac{\partial^3 u}{\partial x \partial y^2} + B_{22}\dfrac{\partial^3 v}{\partial y^3} - (B_{12}+2B_{66})\dfrac{\partial^3 v}{\partial x^2 \partial y} - D_{11}\dfrac{\partial^4 w_b}{\partial x^4} \\ -2(D_{12}+2D_{66})\dfrac{\partial^4 w_b}{\partial x^2 \partial y^2} - D_{22}\dfrac{\partial^4 w_b}{\partial y^4} - D^s_{11}\dfrac{\partial^4 w_s}{\partial x^4} - 2\left(D^s_{12}+2D^s_{66}\right)\dfrac{\partial^4 w_s}{\partial x^2 \partial y^2} \\ -D^s_{22}\dfrac{\partial^4 w_s}{\partial y^4} - I_0\dfrac{\partial^2 (w_b+w_s)}{\partial t^2} - I_1\left(\dfrac{\partial^2 u}{\partial x \partial t^2} + \dfrac{\partial^2 v}{\partial y \partial t^2}\right) + I_2\nabla^2\dfrac{\partial^2 w_b}{\partial t^2} \\ +J_2\nabla^2\dfrac{\partial^2 w_s}{\partial t^2} + \left(k_p - N^T\right)\nabla^2(w_b+w_s) - k_w(w_b+w_s) = q_{dynamic} \end{cases} \tag{47}$$

$$\begin{cases} B^s_{11}\dfrac{\partial^3 u}{\partial x^3} + \left(B^s_{12}+2B^s_{66}\right)\dfrac{\partial^3 u}{\partial x \partial y^2} + B^s_{22}\dfrac{\partial^3 v}{\partial y^3} - \left(B^s_{12}+2B^s_{66}\right)\dfrac{\partial^3 v}{\partial x^2 \partial y} - D^s_{11}\dfrac{\partial^4 w_b}{\partial x^4} \\ -2\left(D^s_{12}+2D^s_{66}\right)\dfrac{\partial^4 w_b}{\partial x^2 \partial y^2} - D^s_{22}\dfrac{\partial^4 w_b}{\partial y^4} - H^s_{11}\dfrac{\partial^4 w_s}{\partial x^4} - 2\left(H^s_{12}+2H^s_{66}\right)\dfrac{\partial^4 w_s}{\partial x^2 \partial y^2} \\ -H^s_{22}\dfrac{\partial^4 w_s}{\partial y^4} + A^s_{44}\nabla^2 w_s - I_0\dfrac{\partial^2 (w_b+w_s)}{\partial t^2} - J_1\left(\dfrac{\partial^2 u}{\partial x \partial t^2} + \dfrac{\partial^2 v}{\partial y \partial t^2}\right) \\ +J_2\nabla^2\dfrac{\partial^2 w_b}{\partial t^2} + K_2\nabla^2\dfrac{\partial^2 w_s}{\partial t^2} + \left(k_p - N^T\right)\nabla^2(w_b+w_s) - k_w(w_b+w_s) = q_{dynamic} \end{cases} \tag{48}$$

Table 3
Comparison of the dimensionless natural frequency (Ω) of the square metal plate with different side to thickness ratio and various B.Cs ($\Omega = \omega\left(\frac{b}{\pi}\right)^2\sqrt{\frac{\rho h}{D^*}}$).

B.Cs	a/h	Mode	Porosity coefficient (e_1)									
\			0.1		0.2		0.3		0.4		0.5	
			Present	Ref [76]	Present	Ref [76]	Present	Ref [76]	Present	Ref [76]	Present	Ref [76]
SSSS	100	1	1.9956	1.9956	1.9937	1.9937	1.9941	1.9941	1.9977	1.9978	2.0059	2.0060
SSSS	100	2	4.9862	4.9866	4.9813	4.9817	4.9821	4.9826	4.9910	4.9916	5.0112	5.0120
SSSS	10	1	1.9257	1.9265	1.9218	1.9228	1.9178	1.9210	1.9179	1.9220	1.9192	1.9269
SSSS	10	2	4.5874	4.5912	4.5675	4.5768	4.5499	4.5662	4.5353	4.5612	4.5371	4.5642
CCCC	100	1	3.7610	3.6351	3.7573	3.6316	3.7579	3.6322	3.7646	3.6387	3.7798	3.6535
CCCC	100	2	7.3021	7.4083	7.2895	7.4007	7.2933	7.4017	7.3015	7.4146	7.3010	7.4444
CCCC	10	1	3.4710	3.2813	3.4554	3.2690	3.4413	3.2591	3.4294	3.2529	3.4204	3.2520
CCCC	10	2	6.2532	6.2505	6.2146	6.2175	6.1863	6.1881	6.1625	6.1639	6.1453	6.1478

Table 4
Comparison of the dimensionless natural frequency of the square metal plate without considering porosities and with respect to various B.Cs, side-to-thickness ratio and mode numbers ($\Omega = \omega\left(\frac{b}{\pi}\right)^2\sqrt{\frac{\rho h}{D^*}}$).

a/h	Mode	B.Cs					
		SSSS	SSSS	SSSS	CCCC	CCCC	CCCC
		Present	Ref [76]	Ref [77]	Present	Ref [76]	Ref [77]
100	1	1.999272	1.9993	1.9993	3.667992	3.6419	3.6420
100	2	4.995455	4.9958	4.9955	7.492145	7.4222	7.4214
10	1	1.931721	1.9317	1.9319	3.387646	3.2954	3.3092
10	2	4.608808	4.6084	4.6098	6.318872	6.2859	6.3317

Table 5
Comparison of the fundamental natural frequencies of epoxy square plate reinforced with GPLs under SSSS boundary condition by considering different GPL distribution patterns and various mode numbers ($\Omega = \omega h\sqrt{\frac{\rho_m}{E_m}}$, h = a/10, a = b = 0.45 m, W_{GPL} = 1%).

Mode numbers (m,n)	GPL distribution pattern								
	FG-O	FG-O	FG-O	UD	UD	UD	FG-X	FG-X	FG-X
	Present	Ref [28]	Ref [35]	Present	Ref [28]	Ref [35]	Present	Ref [28]	Ref [35]
(1,1)	0.0966	0.097	0.102	0.1216	0.121	0.122	0.1388	0.141	0.138
(2,1)	0.2345	0.234	0.246	0.2895	0.289	0.290	0.3242	0.331	0.325
(2,2)	0.3634	0.363	0.380	0.4437	0.443	0.444	0.4866	0.503	0.494

3. Solution procedure

Herein, the governing equations (45)-(48) will be analytically solved with an exact solution to achieve the natural frequencies of the GOPRMF nanocomposite plate. For this aim, the well-known Galerkin's method is employed which one of the best and accurate solution techniques for the vibration problems. In this investigation, various B.Cs such as simply-supported (S–S–S–S), fully clamped (C–C–C–C) or the combination of them are considered which are given as Sobhy [80]:

For S–S–S–S plate

$$\begin{cases} At\ x = 0, a\ N_x = M_x = w_b = w_s = 0 \\ At\ y = 0, b\ N_y = M_y = w_b = w_s = 0 \end{cases} \tag{49}$$

For C–C–C–C plate

$$\begin{cases} At\ x = 0, a\ u = v = w_b = w_s = 0 \\ At\ x = 0, a\ u = v = w_b = w_s = 0 \end{cases} \tag{50}$$

According to Galerkin's method, the displacement functions of the plate which satisfy the above-mentioned B.Cs can be stated as

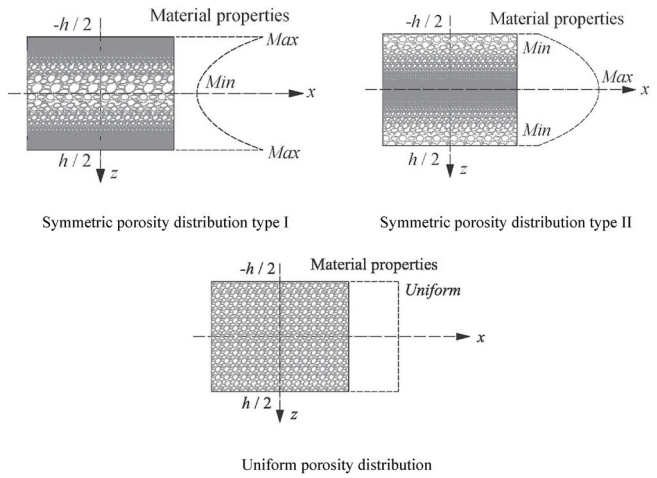

Fig. 2. Various porosity distribution of the metal foam plate.

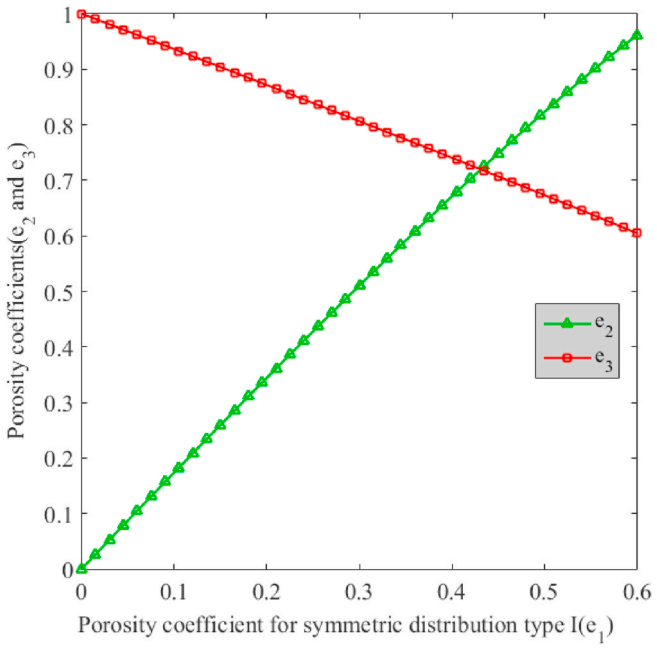

Fig. 3. Variation of porosity coefficient (e_2 and e_3) of GOPRMF nanocomposite plate versus porosity coefficient for symmetric distribution type I (e_1).

follows:

$$u = \sum_{m=1}^{\infty}\sum_{n=1}^{\infty} U_{mn}\frac{\partial X_m(x)}{\partial x}Y_n(y)e^{i\omega_n t} \tag{51a}$$

$$v = \sum_{m=1}^{\infty}\sum_{n=1}^{\infty} V_{mn}\frac{\partial Y_n(y)}{\partial y}X_m(x)e^{i\omega_n t} \tag{51b}$$

$$w_b = \sum_{m=1}^{\infty}\sum_{n=1}^{\infty} W_{bmn}Y(y)X_m(x)e^{i\omega_n t} \tag{51c}$$

$$w_s = \sum_{m=1}^{\infty}\sum_{n=1}^{\infty} W_{smn}Y_n(y)X_m(x)e^{i\omega_n t} \tag{51d}$$

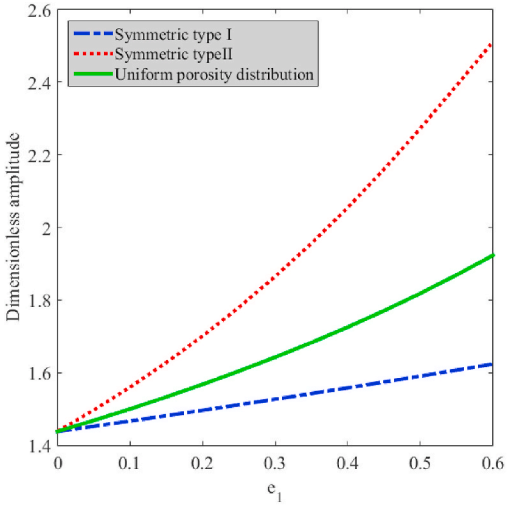

(a) S-S-S-S boundary condition

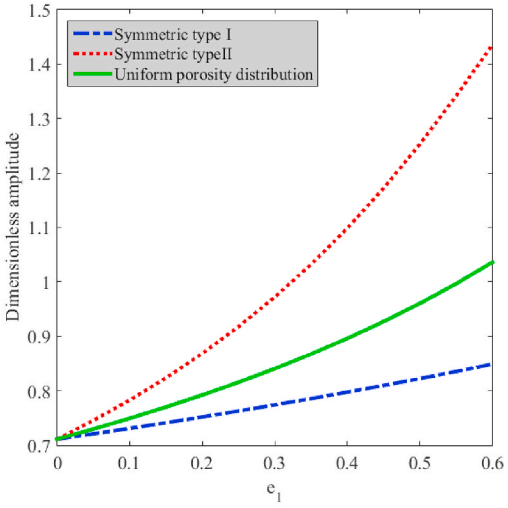

(b) C-C-S-S boundary condition

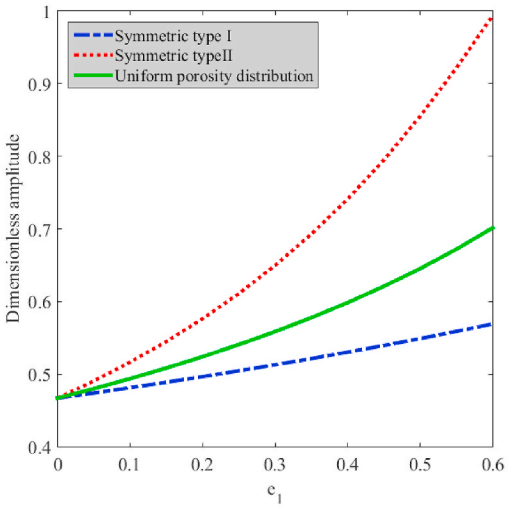

(c) C-C-C-C boundary condition

Fig. 4. Influence of various porosity distribution (type I, II and uniform) on the dimensionless amplitude of GOPRMF nanocomposite plate for (a) S–S–S–S, (b) S–S–C–C and (c) C–C–C–C boundary conditions.

where U_{mn}, V_{mn}, W_{smn} and W_{bmn} are the unknown coefficients. Also, $X_m(x)$ and $Y_n(y)$ are two trigonometric functions which are varied with respect to various B.Cs. These functions can be found in Table 2 for different B.Cs $\left(\alpha = \frac{m\pi}{a}, \beta = \frac{n\pi}{b}\right)$. Now, by inserting Eq. (51) into Eq.(45)-(48) and employing Galerkin solution method, one obtains:

$$\left([K]_{4\times4} - \omega_{ex}^2[M]_{4\times4}\right)\begin{bmatrix} U_{mn} \\ V_{mn} \\ W_{bmn} \\ W_{smn} \end{bmatrix} = \begin{bmatrix} 0 \\ 0 \\ Q_{dynamic} \\ Q_{dynamic} \end{bmatrix} \tag{52}$$

in which ω_{ex} is the excitation frequency. The formulation of the $Q_{dynamic}$ and components of the stiffness and mass matrices can be found in the Appendix of this paper. Given that the structure is subjected to uniform transverse dynamic loading acting harmonically along a straight line, this dynamic load are stated as follows:

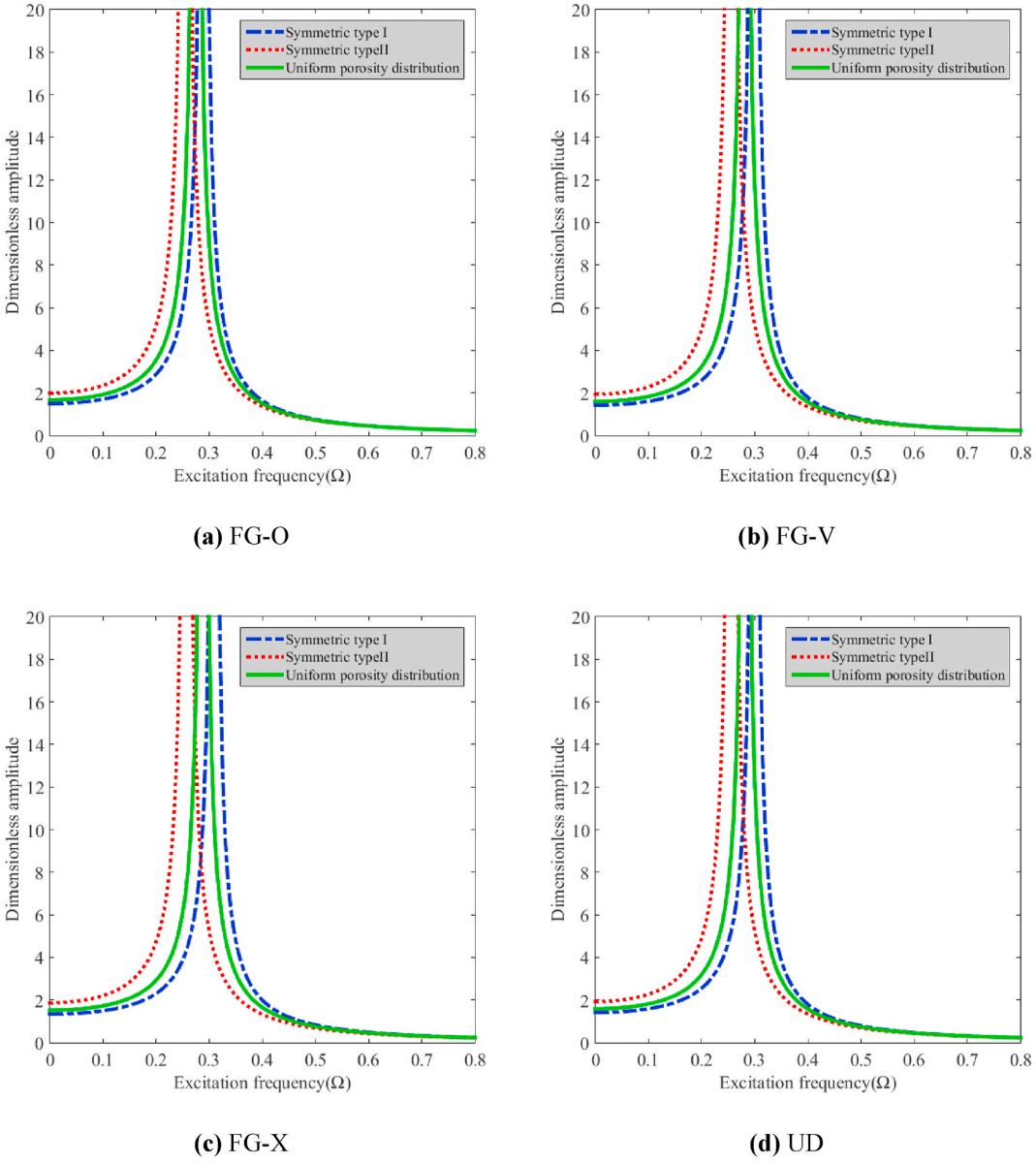

Fig. 5. Variation of dimensionless amplitude of GOPRMF nanocomposite plate against excitation frequency (Ω) with considering various types of porosity distribution for different patterns of dispersing reinforcement powders such as (a) FG-O, (b) FG-V, (c) FG-X and (d) UD.

$$q_{dynamic} = \sum_{n=1}^{\infty} Q_n \sin(\alpha x)\sin(\beta y)\sin(\omega t) \tag{53}$$

$$\begin{aligned} Q_n &= \frac{4q_0}{mn}\int_{x_0+0.5a_0}^{x_0+0.5a_0}\int_{y_0+0.5b_0}^{y_0+0.5b_0}\sin(\alpha x)\sin(\beta y)q(x)dxdy \\ &= \frac{16q_0}{mn\pi^2}\sin(\alpha x_0)\sin\left(\frac{m\pi a_0}{2a}\right)\sin(\beta y_0)\sin\left(\frac{m\pi b_0}{2b}\right) \end{aligned} \tag{54}$$

where in above equation, $q(x) = q_0$ and q_0 is the density of the uniform dynamic loading. Also, Q_n, x_0 and y_0 denote the Fourier coefficients and centroid coordinates respectively.

4. Verification studies

In order to validate the results of this study, the natural frequency responses are compared with some previous works in this field.

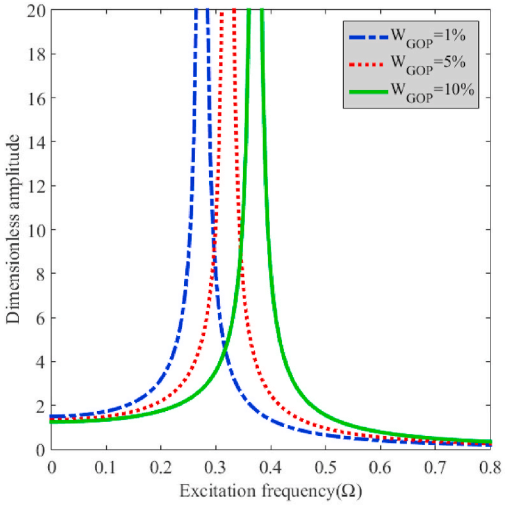

(a) S-S-S-S boundary condition

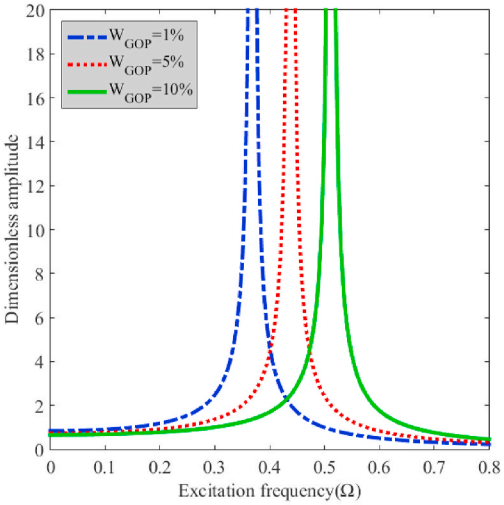

(b) C-C-S-S boundary condition

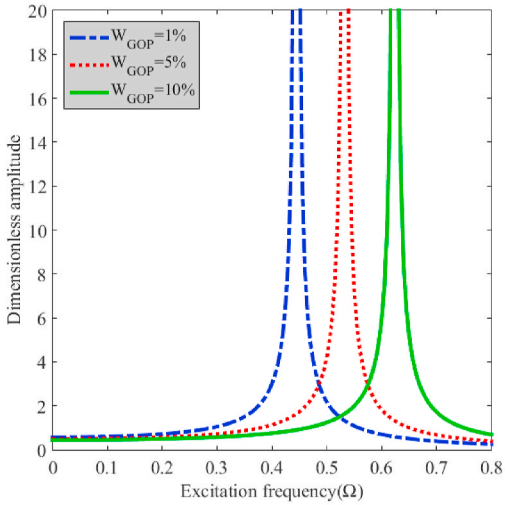

(c) C-C-C-C boundary condition

Fig. 6. The effect of different values of weight fraction of GOP (w_{GOP}) on the dimensionless amplitude of GOPRMF nanocomposite plate against excitation frequency (Ω) with respect to (a) S–S–S–S, (b) C–C–S–S and (c) C–C–C–C boundary conditions.

For this purpose, three tables are provided to prove the accuracy of the methodology employed in different parts of the current paper. First of all, the first two dimensionless natural frequencies of the porous plates are tabulated in Table 3 with considering different values of side-to-thickness ratio and various B.Cs. The porosity distribution is supposed to be symmetric type I with a variable coefficient. By comparing the results of this paper and those reported by Xue et al. [81] which have been achieved using isogeometric approach, a perfect agreement can be observed.

Also, the validity of the present solution method can be realized from Table 4, where the results of the present paper agree well with those obtained by Mahi and Tounsi [82] and Xue et al. [81] for the perfect square metal plates made of steel. In these works, the Ritz and the Gauss quadrature methods were utilized respectively as solution techniques which are completely different from what we used in our paper, thus the validation of the proposed method of the solution will be proved.

Moreover, the correctness of the refine higher order plate theory and the methodology used for various FG patterns will be verified by investigating the results listed in Table 5. In this table the reference results [31,38] for dimensionless natural frequencies were calculated on the basis of the FSDT. A reliable agreement are achieved in this table which can confirm the validity of the presented theory and FG patterns.

According to this section, it would be clear that the present study can efficiently estimate the vibrational responses of the GOPRMF

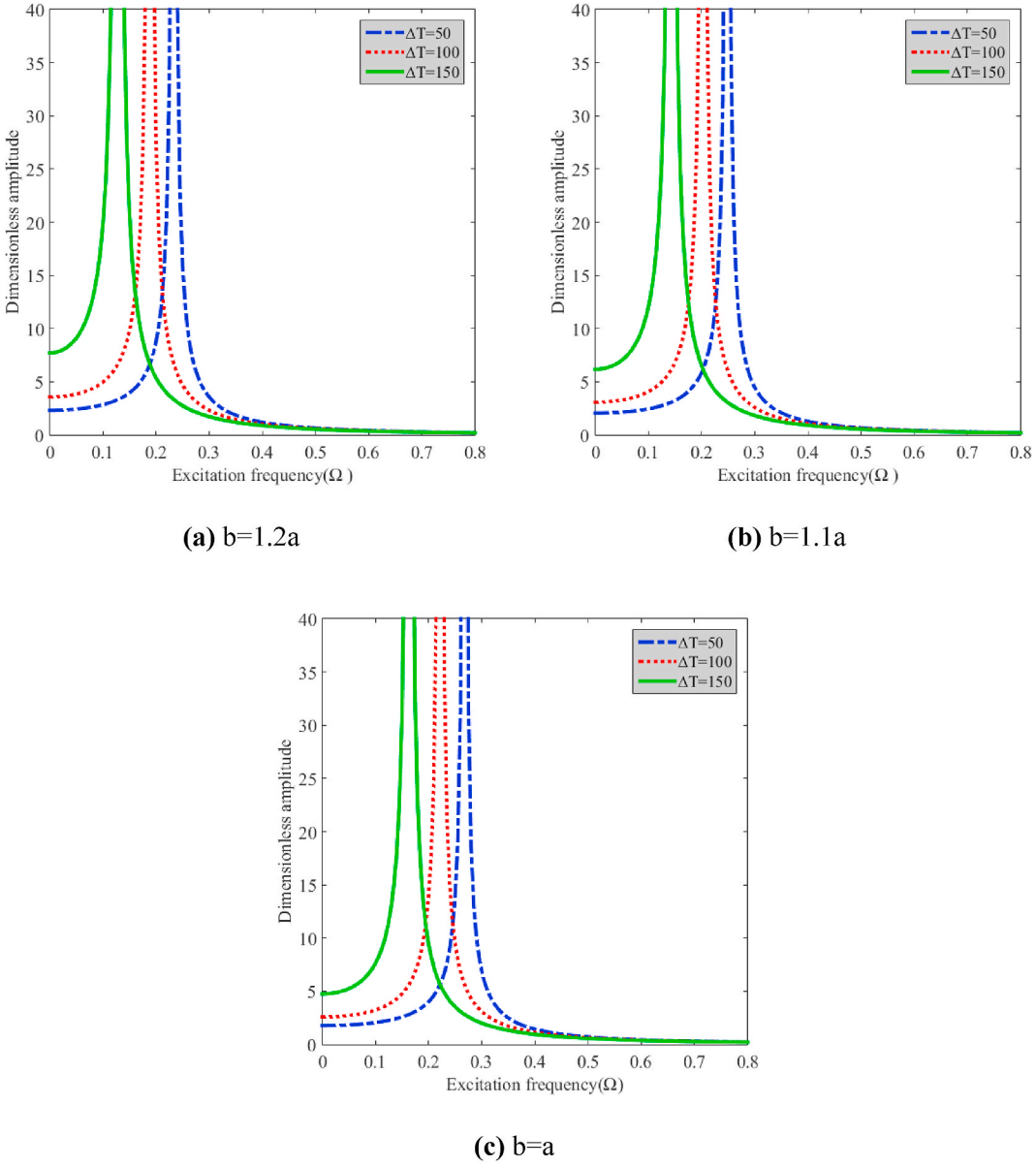

Fig. 7. Variation of dimensionless amplitude of GOPRMF nanocomposite plate with considering different values of temperature change (ΔT) versus excitation frequency (Ω) with respect to (a) b = 1.2a, (b) b = 1.1a and (c) b = a.

nanocomposite plates.

5. Numerical results and discussion

This part is assigned to some depicted numerical results to investigate the forced vibration behavior of GOPRMF nanocomposite plates subjected to a uniformly applied dynamic load, uniform type of thermal loadings, and also rested on elastic Winkler-Pasternak foundation. Herein, to explore that, how various parameters, for instance, disparate kinds of GO reinforcement's distribution, the weight fraction of GOPs, the aspect ratio, length to thickness ratio, different values of temperature change and also two sorts of elastic foundation. By solving Eq. (52) the shear (W_{sn}) and bending (W_{bn}) displacements will be obtained. With having these displacements, the dynamic amplitude or dynamic deflection of the GOPRMF plate can be derived by $W = W_{sn} + W_{bn}$. Owing to simplicity, the non-dimensional form of the excitation frequency, Winkler-Pasternak parameters and dynamic amplitude are presented as below:

$$\Omega = \omega_{ex} a \left(\frac{\rho_M}{E_M}\right)^{0.5}, \quad \widetilde{\mathrm{D}} = \frac{E_M h^3}{12(1-\nu_M^2)}, \quad K_w = k_w \frac{a^4}{\widetilde{D}}, \quad K_p = k_p \frac{a^4}{\widetilde{D}}, \quad \overline{W}_{uniform} = W \frac{10 E_M h^3}{a^4 q_0}$$

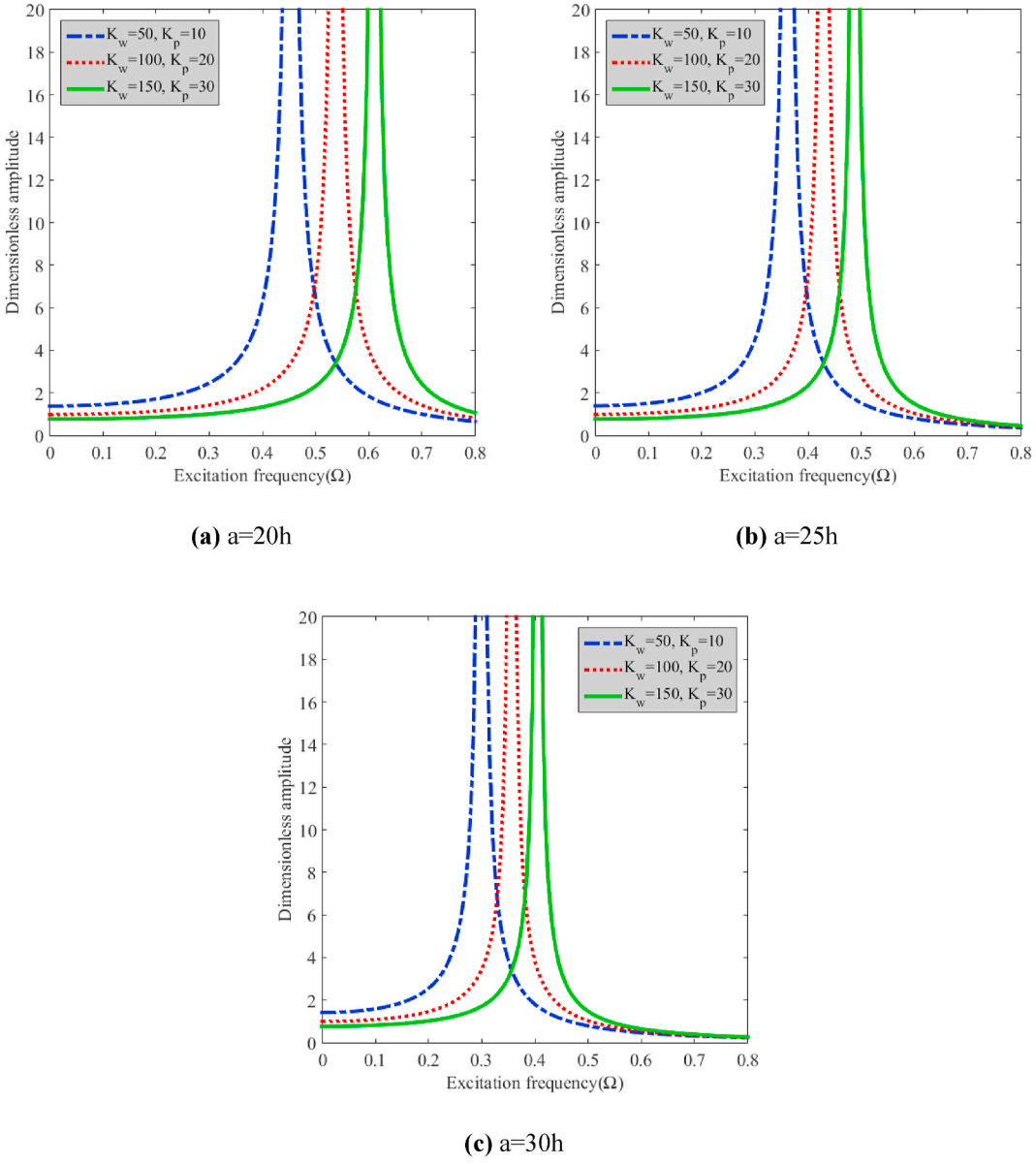

Fig. 8. Efficacy of simultanouse effects of Winkler (K_w) and Pasternak (K_p) foundation coefficients on dimensionless amplitude of GOPRMF nanocomposite plate against excitation frequency (Ω) with respect to (a) a = 20h, (b) a = 25h and (c) a = 30h

in which, ω_{mn} indicates the natural frequency of the GOPRMF nanocomposite plate and the mode number in the x and y direction indicated by m and n, respectively. Moreover, the material characteristics of the constituent materials brought in Table 1. Also, the geometry of the plate embedded on an elastic substrate presented in Figs. 1 and 2.

For the sake of the verity that the entire mass of GOPRMF reinforced nanocomposite plates by considering different kinds of porosity or GOP dispersion are equivalent, the relation between various types of porosity coefficients is studied by considering Equation. (15). Afterward, in order to study the variation of porosity coefficient of GOPRMF nanocomposite plate against porosity coefficient for symmetric distribution type I (e_1), Fig. 3 is reported. It is obvious that, by increasing in e_1 values, the porosity coefficient e_2 increases, whiles, the porosity coefficient e_3 decreases (e_1 and e_3 in opposite to e_1 and e_2 are inversely related).

The influence of various porosity distribution (type I, II and uniform) on the dimensionless amplitude of GOPRMF nanocomposite plate for S–S–S–S, S–S–C–C and C–C–C–C boundary conditions are depicted in Fig. 4. It can be seen that; the simply supported (S–S–S–S) boundary condition includes the higher values of dimensionless amplitude and also the fully clamped (C–C–C–C) boundary condition possesses the lower values of mentioned parameter compared with the other type (S–S–C–C), which means that the C–C–S–S boundary condition owns the middle values of dimensionless frequency for all types of porosity distribution. Furthermore, it is obvious

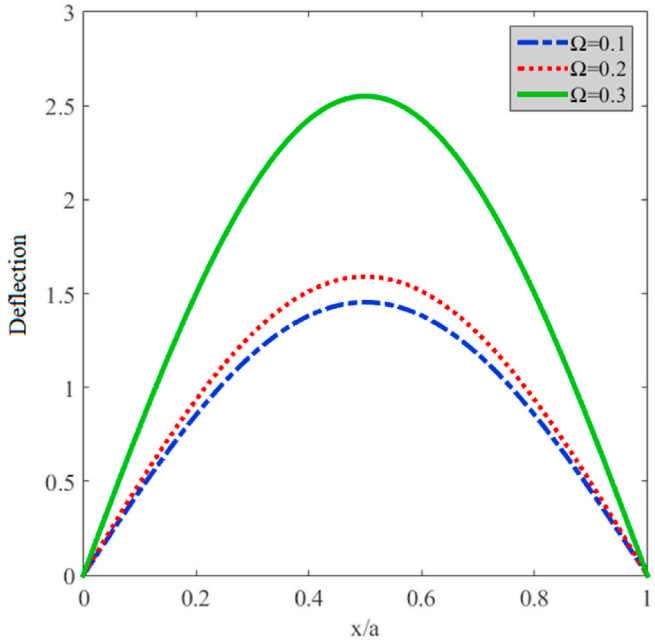

Fig. 9. Mode shape of the GOPRMF nanocomposite plate for different values of excitation frequency (Ω).

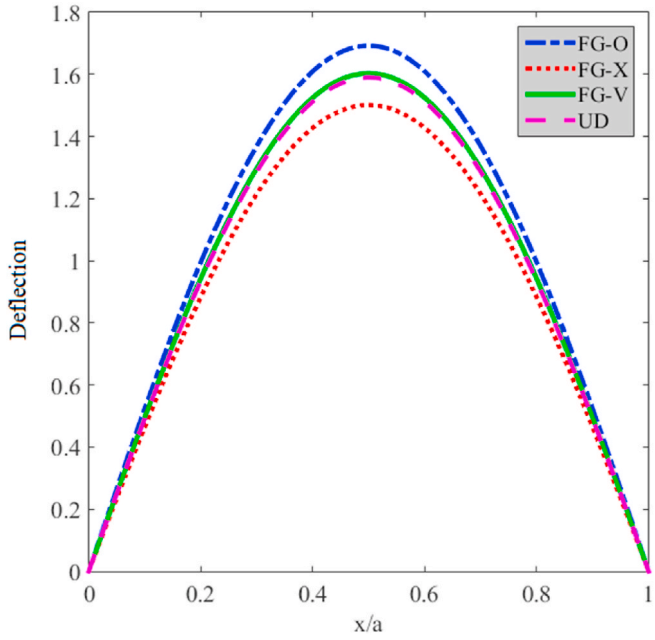

Fig. 10. Mode shape of the GOPRMF nanocomposite plate for different types of distributing GO reinforcement powders.

that, increasing in the porosity coefficient of symmetric distribution type I (e_1) leads to an increase in the dimensionless amplitude values of the GOPRMF nanocomposite plate with porosity distribution type I, II and uniform. It can be concluded that by increasing the porosity coefficient of type I (e_1), a stiffness-softening effect will be occurred and the structure will become more flexible.

It must be mentioned that from this figure to the end, except the parameters defined in the figures, other conditions would be as: S–S–S–S edge condition $W_{GOP} = 3\%, K_p = 10, K_w = 50, \Delta T = 10$, UD pattern for GOPs, Symmetric type I for porosity distribution and $e_1 = 0.5$.

Fig. 5 is devoted to explore the variation of dimensionless amplitude of GOPRMF nanocomposite plate against excitation frequency (Ω) with considering and comparing various types of porosity distribution for different patterns of dispersing reinforcement powders

such as FG-O, FG-V, FG-X and UD. It is clear that increasing in excitation frequency causes an increase in dimensionless amplitude until it attains to the resonance frequency, afterward, the dimensionless frequency will decrease and tends to zero slowly. Also, it can be seen that, before the excitation frequency attains to the natural frequency, in a constant value of excitation frequency and every arbitrary type of GOP distribution pattern, the dimensionless amplitude of type II is highest and type I is the lowest. However, after that the excitation frequency arrives to the natural frequency, behavior of dimensionless amplitude reversed, so that the dimensionless amplitude of type I is highest and type II is the lowest value. It is observable that, the resonance frequency of the considered plate is about the Ω∼0.3. Also however slight, but the resonance frequency has been affected by the various GOP distribution pattern types, and we can recognize that the FG-X distributing pattern leads to a bigger resonance frequency compared to other types of distribution. So that, the FG-O distributing pattern leads to a lower resonance frequency compared to other types of distribution and also FG-V and UD types are very close to each other and have the medium value of resonance frequency. Moreover, in a constant value of excitation frequency, for all types of porosity distributions, the dimensionless frequency of FG-X type is lower than the other patterns.

The effect of different values of weight fraction of GOP (W_{GOP}) on the dimensionless amplitude of GOPRMF nanocomposite plate against excitation frequency (Ω) is illustrated in Fig. 6 with respect to S–S–S–S, C–C–S–S and C–C–C–C boundary conditions. It can be seen that, in all types of boundary condition or W_{GOP} values, increasing in excitation frequency, increases the dimensionless amplitude before resonance and decreases that after resonance frequency. Moreover, it is clear that, in a constant value of dimensionless amplitude, an increase in W_{GOP} values, causes the forward movement of the associated diagram which means that the values of excitation frequency increase. Also, it is obvious that increasing the weight fraction of GOPs is proportional to higher stiffness of material which leads to bigger values of resonance frequency. Consequently, the delay in the occurrence of resonance phenomenon is the result of stiffness hardening happened in the constitutive materials of the structure which is caused by increasing the weight fraction of GOPs as a high strength reinforcement. Also, it is obvious that increase of weight fraction of GOP is proportional to higher stiffness of material which leads to bigger values of resonance frequency. Furthermore, the resonance frequency is significantly affected by type of boundary condition. For instance, it is observable that, the fully clamped (C–C–C–C) boundary condition, regardless of the value of W_{GOP} (for all values of W_{GOP}), possesses highest values of resonance frequency, and on the other hand, the fully simply supported (S–S–S–S) boundary condition, for all values of W_{GOP}, possesses lowest values of resonance frequency. In addition, it is indicated that, in the fully clamped boundary condition, the curves corresponding to each W_{GOP} are more distinguished from each other, and also, in the fully simply supported boundary condition, the curves corresponding to each W_{GOP} are less distinguished from each other.

Fig. 7 indicates the variation of dimensionless amplitude of GOPRMF nanocomposite plate with considering different values of temperature change (ΔT) versus excitation frequency (Ω) with respect to $b = 1.2a$, $b = 1.1a$ and $b = a$ values. It is obvious that, before the excitation frequency attains to the natural frequency, in a constant value of excitation frequency, increasing the temperature change will increase the dimensionless amplitude, but after the excitation frequency arrives to the natural frequency, increasing the temperature change will decrease the dimensionless amplitude value. Also, in a constant value of dimensionless frequency, it is indicated that, increasing in temperature change, decreases the resonance frequency directly since applying the thermal loadings with higher with higher temperatures will soften the materials and reduce the stiffness of the structure. In addition, we can see that increasing in b/a ratio, leads to a decrease in resonance frequency, regardless of the value of temperature change. As the aspect ratio of the proposed plate increases, this trend can be observable when the sides of the plate become larger unequally.

Fig. 8 is devoted to investigate the efficacy of simultaneous effects of Winkler (K_w) and Pasternak (K_p) foundation coefficients on dimensionless amplitude of GOPRMF nanocomposite plate against excitation frequency (Ω) with respect to $a = 20h$, $a = 25h$ and $a = 30h$ values. It is clearly shown that, increasing in a/h ratio leads to decrease in resonance frequency, regardless of the values of Winkler and Pasternak coefficients. Also, in each diagram that is dedicated to a specific value of a/h ratio, it can be seen that, in a constant value of dimensionless amplitude, resonance frequency gets bigger when the foundation's coefficients increase. Since the interaction between the plate and Pasternak layer of the foundation is more continuously, this layer affect the vibrational response of the structure remarkably in comparison with Winkler springs. Moreover, in a constant value of excitation frequency before the resonance frequency, increasing in Winkler and Pasternak coefficients leads to a decrease in associated dimensionless amplitude, unlike after the resonance frequency situation. Furthermore, it is clear that, by decreasing the a/h value, the curves corresponding to each foundation's coefficients are more distinguished from each other.

The influence of different values of excitation frequency (Ω) on the first mode shape of the GOPRMF nanocomposite plate is presented in Fig. 9. It is observable that, increasing in x/a ratio leads to an increase and then decrease in dimensionless amplitude such as a downward parabola. Also, one can see that increasing the value of excitation frequency causes to increase in the associated deflection. In other words, higher excitation frequency causes higher flexibility in the structure's behavior.

Fig. 10 is dedicated to analyzing the mode shape of the GOPRMF nanocomposite plate for different types of distributing GO reinforcement powders. It is clear that the deflection's values from highest to lowest can be arranged in the order of: FG-O, FG-V, UD, and FG-X. Hence, we can say that the FG-O distribution type possesses the highest value of deflection which means that the FG-O distribution pattern makes the structure more flexible, and unlike, the FG-X distribution type is less flexible due to the fact that this pattern owns the lowest values of deflection. The reason that the FG-X pattern has the highest effect in making the structure stiffer, can be concluded in this statement that this pattern can counteract the influence of maximum moments in edges of the plate by having the most amounts of nanofillers in these places. With this concept, it would be comprehensible that why the structure with this pattern has the lowest values of deflection which is followed by UD, V and O patterns. In addition, it can be seen that the highest deflection is occurred at the center of the plate.

6. Conclusion

This paper is dedicated to analyzing the forced vibration behavior of the GOPRMF nanocomposite plate, in which the considered plate is subjected to a uniform dynamic load and embedded on an elastic foundation. The shear deformation efficacy is involved by employing the refined higher-order shear deformation theory. Various through the thickness porosity distribution types, various GOPs' distribution patterns, and different B.Cs were taken into consideration. Additionally, the framework of Hamilton's principle is implemented to achieve the forced vibrational governing equations of motion and afterward these equations were analytically solved by utilizing Galerkin's approach for all considered B.Cs. Afterward, the change of the dimensionless amplitude of the GOPRMF nanocomposite plate was demonstrated in disparate graphical results regarding the influences of various parameters which were completely described in the previous section. Moreover, in order to characterize these consequences and the influences on the forced vibrational demeanor, a complete discussion was reported. Finally, some important results were obtained, that can be highlighted as below:

Porosity distribution type II and the simply supported B.C led to highest values of deflection compared to other distribution and B.C types.
The GOPs' distribution patterns could affect strongly the deflection and slightly on the resonance frequency of the structure in the way that the FG-X pattern had the highest values of resonance frequency and lowest values of deflection and the FG-O pattern got these values completely reverse.
Increase in the amounts of GOPs' weight fraction is proportional to higher stiffness of material which leads to higher values of resonance frequency.
Resonance frequency gets bigger when the foundation's coefficients increase.

Declaration of competing interest

The authors declare that they have no known competing financial interests or personal relationships that could have appeared to influence the work reported in this paper.

Acknowledgment

This research is financially supported by the Ministry of Science and Technology of China (Grant No. 2019YFE0112400), National Science Foundation of China (Grant No. 51678322), the Taishan Scholar Priority Discipline Talent Group program funded by the Shan Dong Province, and the first-class discipline project funded by the Education Department of Shandong Province. The publication of this article was funded by Qatar National Library.

Appendix

The components of the stiffness matrix are as follows:

$$k_{11} = A_{11}r_1 + A_{66}r_2,\ k_{12} = (A_{12} + A_{66})r_2,\ k_{13} = -B_{11}r_1 - (B_{11} + 2B_{66})r_2$$
$$k_{14} = B^s_{11}r_1 - \left(B^s_{11} + 2B^s_{66}\right)r_2,\ k_{21} = (A_{12} + A_{66})r_3, k_{22} = A_{22}r_4A_{66}r_3$$
$$k_{23} = -B_{22}r_4 - (B_{12} + 2B_{66})r_3,\ k_{24} = -B^s_{22}r_4 - \left(B^s_{12} + 2B^s_{66}\right)r_1$$
$$k_{31} = B_{11}r_5 + (B_{12} + 2B_{66})r_6,\ k_{32} = B_{22}r_7 + (B_{12} + 2B_{66})r_6$$
$$k_{33} = -D_{11}r_5 - 2(D_{12} + 2D_{66})r_6 - D_{22}r_7 - k_wr_8 + \left(k_p - N_T\right)(r_{10} + r_9)$$
$$k_{34} = -D^s_{11}r_5 - 2\left(D^s_{12} + 2D^s_{66}\right)r_6 - D^s_{22}r_7 - k_wr_8 + \left(k_p - N_T\right)(r_{10} + r_9)$$
$$k_{41} = B^s_{11}r_5 + \left(B^s_{11} + 2B^s_{66}\right)r_6,\ k_{42} = B^s_{22}r_7 + \left(B^s_{12} + 2B^s_{66}\right)r_6$$
$$k_{43} = -D^s_{11}r_5 - 2\left(D^s_{12} + 2D^s_{66}\right)r_6 - D^s_{22}r_7 - k_wr_8 + \left(k_p - N_T\right)(r_{10} + r_9)$$
$$k_{44} = -H^s_{11}r_5 - 2\left(H^s_{12} + 2H^s_{66}\right)r_6 - H^s_{22}r_7 - k_wr_8 + \left(A^s + k_p - N_T\right)(r_{10} + r_9)$$

The components of the mass matrix are defined as:

$$m_{11} = I_0r_{11},\ m_{12} = 0,\ m_{13} = -I_1r_{11},\ m_{14} = -J_1r_{11}$$
$$m_{21} = 0,\ m_{22} = I_0r_{12},\ m_{23} = -I_1r_{12},\ m_{24} = -J_1r_{12}$$
$$m_{31} = -I_1r_{10},\ m_{32} = I_1r_9,\ m_{33} = I_0r_8 - I_2(r_{10} + r_9)$$
$$m_{34} = I_0r_8 + J_2(r_{10} + r_9),\ m_{41} = -J_1r_{10},\ m_{42} = J_1r_9$$
$$m_{43} = I_0r_8 - J_2(r_{10} + r_9),\ m_{44} = I_0r_8 - K_2(r_{10} + r_9)$$

where

$$\{r_1, r_2, r_{11}\} = \int_0^a \int_0^b X_m'(x)Y_n(y)\{X_m'''(x)Y_n(y), X_m'(x)Y_n''(y), X_m'(x)Y_n(y)\}$$

$$\{r_3, r_4, r_{12}\} = \int_0^a \int_0^b X_m(x)Y_n'(y)\{X_m''(x)Y_n'(y), X_m(x)Y_n'''(y), X_m(x)Y_n'(y)\}$$

$$\{r_5, r_6, r_7\} = \int_0^a \int_0^b X_m(x)Y_n(y)\{X_m''''(x)Y_n(y), X_m''(x)Y_n'''(y), X_m(x)Y_n''''(y)\}$$

$$\{r_8, r_9, r_{10}\} = \int_0^a \int_0^b X_m(x)Y_n(y)\{X_m(x)Y_n(y), X_m(x)Y_n''(y), X_m''(x)Y_n(y)\}$$

Also $Q_{dynamic}$ is expressed as:

$$Q_{dynamic} = Q_n r_8$$

Author statement

Name Email Affiliation author (1) Jie Zheng zhengjie@qut.edu.cn Structural Vibration Control Group, Qingdao University of Technology, Qingdao 266033, China author (2) Chunwei Zhang zhangchunwei@qut.edu.cn Structural Vibration Control Group, Qingdao University of Technology, Qingdao 266033, China author (3) Farayi Musharavati farayi@qu.edu.qa Department of Mechanical and Industrial Engineering Qatar University, Qatar University, P.O. Box 2713, Doha, Qatar; author (4) Afrasyab Khan khana@susu.ru Institude of Engineering and Technology, Department of Hydraulics and Hydraulic and Pneumatic Systems, South Ural State University, Lenin Prospect 76, Chelyabinsk, 454080, Russian Federation (A.K.)author (5) Tamer A. Sebaey sepaey@hotmail.com -Engineering Management Department, College of Engineering, Prince Sultan University, Riyadh, Saudi Arabia -Mechanical Design and Production Department, Faculty of Engineering, Zagazig University, P.O. Box 44519, Zagazig, Sharkia, Egyptauthor (6) Arameh Eyvazian eyvazian@qu.edu.qa Structural Vibration Control Group, Qingdao University of Technology, Qingdao 266033, China.

Please list all the author's Contribution here:

Author's contribution

Author (1): Conceptualization, methodology, formal analysis, investigation, writing—original draft preparation, writing—review author (2): Conceptualization, validation, formal analysis, writing—original draft preparation, editing author (3): methodology, writing—review, software, validation, formal analysis, writing—original draft preparation, writing—review, editing author (4): methodology, investigation, editing author (5):methodology, software, formal analysis, writing—original draft preparation, writing—review, editing author (6):methodology, software, formal analysis, writing—original draft preparation, writing—review, editing.

Contributor roles taxonomy (CRediT)

Conceptualization Ideas; formulation or evolution of overarching research goals and aims. Data curation Management activities to annotate (produce metadata), scrub data and maintain research data (including software code, where it is necessary for interpreting the data itself) for initial use and later re-use. Formal analysis Application of statistical, mathematical, computational, or other formal techniques to analyze or synthesize study data. Funding acquisition of the financial support for the project leading to this publication. Investigation Conducting a research and investigation process, specifically performing the experiments, or data/evidence collection. Methodology Development or design of methodology; creation of models. Project administration Management and coordination responsibility for the research activity planning and execution. Resources Provision of study materials, reagents, materials, patients, laboratory samples, animals, instrumentation, computing resources, or other analysis tools. Software Programming, software development; designing computer programs; implementation of the computer code and supporting algorithms; testing of existing code components. Supervision Oversight and leadership responsibility for the research activity planning and execution, including mentorship external to the core team. Validation Verification, whether as a part of the activity or separate, of the overall replication/reproducibility of results/experiments and other research outputs. Visualization Preparation, creation and/or presentation of the published work, specifically visualization/data presentation. Writing - original draft Preparation, creation and/or presentation of the published work, specifically writing the initial draft (including substantive translation). Writing - review & editing Preparation, creation and/or presentation of the published work by those from the original research group, specifically critical review, commentary or revision – including pre- or post-publication stages.

References

[1] K. Magnucki, P. Stasiewicz, Elastic buckling of a porous beam, J. Theor. Appl. Mech. 42 (2004) 859–868.
[2] B. Smith, et al., Steel foam for structures: a review of applications, manufacturing and material properties, J. Constr. Steel Res. 71 (2012) 1–10.
[3] D. Chen, J. Yang, S. Kitipornchai, Free and forced vibrations of shear deformable functionally graded porous beams, Int. J. Mech. Sci. 108 (2016) 14–22.
[4] M. Jabbari, et al., Buckling analysis of a functionally graded thin circular plate made of saturated porous materials, J. Eng. Mech. 140 (2014) 287–295.
[5] A. Rezaei, A. Saidi, Application of Carrera Unified Formulation to study the effect of porosity on natural frequencies of thick porous–cellular plates, Compos. B Eng. 91 (2016) 361–370.

[6] Y.Q. Wang, C. Liang, J.W. Zu, Examining wave propagation characteristics in metal foam beams: Euler–Bernoulli and Timoshenko models, J. Braz. Soc. Mech. Sci. Eng. 40 (2018) 565.
[7] P. Jasion, et al., Global and local buckling of sandwich circular and beam-rectangular plates with metal foam core, Thin-Walled Struct. 61 (2012) 154–161.
[8] B. Safaei, The effect of embedding a porous core on the free vibration behavior of laminated composite plates, Steel Compos. Struct. 35 (2020) 659–670.
[9] J. Liu, et al., Experimental investigation on the dynamic behaviour of metal foam: from yield to densification, Int. J. Impact Eng. 114 (2018) 69–77.
[10] T. Belica, M. Malinowski, K. Magnucki, Dynamic stability of an isotropic metal foam cylindrical shell subjected to external pressure and axial compression, J. Appl. Mech. 78 (2011).
[11] F. Ebrahimi, A. Seyfi, Studying Propagation of Wave of Metal Foam Rectangular Plates with Graded Porosities Resting on Kerr Substrate in Thermal Environment via Analytical Method, Waves in Random and Complex Media, 2020, pp. 1–24.
[12] F. Ebrahimi, A. Seyfi, Studying propagation of wave in metal foam cylindrical shells with graded porosities resting on variable elastic substrate, Eng. Comput. (2020) 1–17.
[13] F. Ebrahimi, M.R. Barati, P. Haghi, Nonlocal thermo-elastic wave propagation in temperature-dependent embedded small-scaled nonhomogeneous beams, The European Physical Journal Plus 131 (2016) 1–13.
[14] F. Ebrahimi, M.R. Barati, P. Haghi, Wave propagation analysis of size-dependent rotating inhomogeneous nanobeams based on nonlocal elasticity theory, J. Vib. Contr. 24 (2018) 3809–3818.
[15] F. Ebrahimi, P. Haghi, A.M. Zenkour, Modelling of thermally affected elastic wave propagation within rotating Mori–Tanaka-based heterogeneous nanostructures, Microsyst. Technol. 24 (2018) 2683–2693.
[16] F. Ebrahimi, P. Haghi, Wave dispersion analysis of rotating heterogeneous nanobeams in thermal environment, Advances in nano research 6 (2018) 21.
[17] S. Sahmani, B. Safaei, Large-amplitude oscillations of composite conical nanoshells with in-plane heterogeneity including surface stress effect, Appl. Math. Model. 89 (2021) 1792–1813.
[18] F. Fan, S. Sahmani, B. Safaei, Isogeometric nonlinear oscillations of nonlocal strain gradient PFGM micro/nano-plates via NURBS-based formulation, Compos. Struct. 255 (2021) 112969.
[19] S. Chandrasekaran, et al., Fracture toughness and failure mechanism of graphene based epoxy composites, Compos. Sci. Technol. 97 (2014) 90–99.
[20] K. Behdinan, et al., Graphene and CNT impact on heat transfer response of nanocomposite cylinders, Nanotechnol. Rev. 9 (2020) 41–52.
[21] G. Formica, W. Lacarbonara, R. Alessi, Vibrations of carbon nanotube-reinforced composites, J. Sound Vib. 329 (2010) 1875–1889.
[22] A. Alibeigloo, A. Emtehani, Static and free vibration analyses of carbon nanotube-reinforced composite plate using differential quadrature method, Meccanica 50 (2015) 61–76.
[23] P. Zhu, Z. Lei, K.M. Liew, Static and free vibration analyses of carbon nanotube-reinforced composite plates using finite element method with first order shear deformation plate theory, Compos. Struct. 94 (2012) 1450–1460.
[24] N. Wattanasakulpong, V. Ungbhakorn, Analytical solutions for bending, buckling and vibration responses of carbon nanotube-reinforced composite beams resting on elastic foundation, Comput. Mater. Sci. 71 (2013) 201–208.
[25] H.-S. Shen, Y. Xiang, Postbuckling of axially compressed nanotube-reinforced composite cylindrical panels resting on elastic foundations in thermal environments, Compos. B Eng. 67 (2014) 50–61.
[26] M. Heshmati, M. Yas, F. Daneshmand, A comprehensive study on the vibrational behavior of CNT-reinforced composite beams, Compos. Struct. 125 (2015) 434–448.
[27] Z. Lei, L. Zhang, K. Liew, Free vibration analysis of laminated FG-CNT reinforced composite rectangular plates using the kp-Ritz method, Compos. Struct. 127 (2015) 245–259.
[28] L. Zhang, K. Liew, J. Reddy, Postbuckling analysis of bi-axially compressed laminated nanocomposite plates using the first-order shear deformation theory, Compos. Struct. 152 (2016) 418–431.
[29] Z. Song, L. Zhang, K. Liew, Dynamic responses of CNT reinforced composite plates subjected to impact loading, Compos. B Eng. 99 (2016) 154–161.
[30] R. Ansari, J. Torabi, M.F. Shojaei, Buckling and vibration analysis of embedded functionally graded carbon nanotube-reinforced composite annular sector plates under thermal loading, Compos. B Eng. 109 (2017) 197–213.
[31] E. Garcia-Macias, L. Rodriguez-Tembleque, A. Saez, Bending and free vibration analysis of functionally graded graphene vs. carbon nanotube reinforced composite plates, Compos. Struct. 186 (2018) 123–138.
[32] A. Pourasghar, Z. Chen, Hyperbolic heat conduction and thermoelastic solution of functionally graded CNT reinforced cylindrical panel subjected to heat pulse, Int. J. Solid Struct. 163 (2019) 117–129.
[33] L.-L. Ke, J. Yang, S. Kitipornchai, Nonlinear free vibration of functionally graded carbon nanotube-reinforced composite beams, Compos. Struct. 92 (2010) 676–683.
[34] A. Fattahi, B. Safaei, N. Ahmed, A comparison for the non-classical plate model based on axial buckling of single-layered graphene sheets, The European Physical Journal Plus 134 (2019) 555.
[35] S. Chatterjee, et al., Size and synergy effects of nanofiller hybrids including graphene nanoplatelets and carbon nanotubes in mechanical properties of epoxy composites, Carbon 50 (2012) 5380–5386.
[36] S.K. Yadav, J.W. Cho, Functionalized graphene nanoplatelets for enhanced mechanical and thermal properties of polyurethane nanocomposites, Appl. Surf. Sci. 266 (2013) 360–367.
[37] J. Yang, H. Wu, S. Kitipornchai, Buckling and postbuckling of functionally graded multilayer graphene platelet-reinforced composite beams, Compos. Struct. 161 (2017) 111–118.
[38] M. Song, S. Kitipornchai, J. Yang, Free and forced vibrations of functionally graded polymer composite plates reinforced with graphene nanoplatelets, Compos. Struct. 159 (2017) 579–588.
[39] C. Feng, S. Kitipornchai, J. Yang, Nonlinear bending of polymer nanocomposite beams reinforced with non-uniformly distributed graphene platelets (GPLs), Compos. B Eng. 110 (2017) 132–140.
[40] S. Qaderi, F. Ebrahimi, A. Seyfi, An investigation of the vibration of multi-layer composite beams reinforced by graphene platelets resting on two parameter viscoelastic foundation, SN Applied Sciences 1 (2019) 399.
[41] D. Liu, et al., Three-dimensional buckling and free vibration analyses of initially stressed functionally graded graphene reinforced composite cylindrical shell, Compos. Struct. 189 (2018) 560–569.
[42] M. Song, J. Yang, S. Kitipornchai, Bending and buckling analyses of functionally graded polymer composite plates reinforced with graphene nanoplatelets, Compos. B Eng. 134 (2018) 106–113.
[43] H.-S. Shen, et al., Nonlinear bending analysis of FG-GRC laminated cylindrical panels on elastic foundations in thermal environments, Compos. B Eng. 141 (2018) 148–157.
[44] F. Ebrahimi, A. Seyfi, Wave propagation response of agglomerated multi-scale hybrid nanocomposite plates, Waves Random Complex Media (2020) 1–25.
[45] F. Ebrahimi, A. Seyfi, Wave Dispersion Analysis of Embedded MWCNTs-Reinforced Nanocomposite Beams by Considering Waviness and Agglomeration Factors, Waves in Random and Complex Media, 2021, pp. 1–20.
[46] F. Ebrahimi, A. Seyfi, Wave propagation response of multi-scale hybrid nanocomposite shell by considering aggregation effect of CNTs, Mech. Base. Des. Struct. Mach. 49 (2021) 59–80.
[47] F. Ebrahimi, A. Seyfi, A. Dabbagh, Wave dispersion characteristics of agglomerated multi-scale hybrid nanocomposite beams, J. Strain Anal. Eng. Des. 54 (2019) 276–289.
[48] F. Ebrahimi, et al., Wave dispersion characteristics of porous graphene platelet-reinforced composite shells, Struct. Eng. Mech. 71 (2019) 99–107.
[49] R. Moradi-Dastjerdi, et al., Buckling behavior of porous CNT-reinforced plates integrated between active piezoelectric layers, Eng. Struct. 222 (2020) 111141.
[50] W. Gao, Z. Qin, F. Chu, Wave propagation in functionally graded porous plates reinforced with graphene platelets, Aero. Sci. Technol. 102 (2020) 105860.
[51] J.R. Potts, et al., Graphene-based polymer nanocomposites, Polymer 52 (2011) 5–25.

[52] P. Li, et al., Preparation and properties of graphene oxide-modified waterborne polyurethane-acrylate hybrids, Polym. Plast. Technol. Eng. 53 (2014) 1408–1416.
[53] M. Mahkam, et al., Preparation of poly (methacrylic acid)–graphene oxide nanocomposite as a pH-sensitive drug carrier through in-situ copolymerization of methacrylic acid with polymerizable graphene, Polym. Plast. Technol. Eng. 54 (2015) 916–922.
[54] A.A. Balandin, et al., Superior thermal conductivity of single-layer graphene, Nano Lett. 8 (2008) 902–907.
[55] W. Cai, et al., Thermal transport in suspended and supported monolayer graphene grown by chemical vapor deposition, Nano Lett. 10 (2010) 1645–1651.
[56] F. Ebrahimi, M. Nouraei, A. Seyfi, Wave Dispersion Characteristics of Thermally Excited Graphene Oxide Powder-Reinforced Nanocomposite Plates, Waves in Random and Complex Media, 2020, pp. 1–29.
[57] C. Gómez-Navarro, M. Burghard, K. Kern, Elastic properties of chemically derived single graphene sheets, Nano Lett. 8 (2008) 2045–2049.
[58] L.-C. Tang, et al., The effect of graphene dispersion on the mechanical properties of graphene/epoxy composites, Carbon 60 (2013) 16–27.
[59] Z. Zhang, et al., Mechanical analysis of functionally graded graphene oxide-reinforced composite beams based on the first-order shear deformation theory, Mech. Adv. Mater. Struct. 27 (2020) 3–11.
[60] F. Ebrahimi, M. Nouraei, A. Dabbagh, Modeling vibration behavior of embedded graphene-oxide powder-reinforced nanocomposite plates in thermal environment, Mech. Base. Des. Struct. Mach. 48 (2020) 217–240.
[61] F. Ebrahimi, M. Nouraei, A. Dabbagh, Thermal vibration analysis of embedded graphene oxide powder-reinforced nanocomposite plates, Eng. Comput. 36 (2020) 879–895.
[62] F. Ebrahimi, A. Dabbagh, Ö. Civalek, Vibration analysis of magnetically affected graphene oxide-reinforced nanocomposite beams, J. Vib. Contr. 25 (2019) 2837–2849.
[63] F. Ebrahimi, et al., Buckling analysis of graphene oxide powder-reinforced nanocomposite beams subjected to non-uniform magnetic field, Struct. Eng. Mech. 71 (2019) 351–361.
[64] F. Ebrahimi, et al., Thermal buckling analysis of embedded graphene-oxide powder-reinforced nanocomposite plates, Advances in nano research 7 (2019) 293–310.
[65] M. Van Es, Polymer-clay Nanocomposites, PhD Thesis., Delft, 2001.
[66] W. Zhang, J. Yang, Y. Hao, Chaotic vibrations of an orthotropic FGM rectangular plate based on third-order shear deformation theory, Nonlinear Dynam. 59 (2010) 619–660.
[67] Y.Q. Wang, Electro-mechanical vibration analysis of functionally graded piezoelectric porous plates in the translation state, Acta Astronaut. 143 (2018) 263–271.
[68] Y. Hao, et al., Nonlinear dynamics of a functionally graded thin simply-supported plate under a hypersonic flow, Mech. Adv. Mater. Struct. 22 (2015) 619–632.
[69] Y.Q. Wang, J.W. Zu, Nonlinear dynamics of a translational FGM plate with strong mode interaction, Int. J. Struct. Stabil. Dynam. 18 (2018) 1850031.
[70] Y. Hao, W. Zhang, J. Yang, Nonlinear oscillation of a cantilever FGM rectangular plate based on third-order plate theory and asymptotic perturbation method, Compos. B Eng. 42 (2011) 402–413.
[71] Y. Hao, et al., Nonlinear oscillations, bifurcations and chaos of functionally graded materials plate, J. Sound Vib. 312 (2008) 862–892.
[72] Y.Q. Wang, J.W. Zu, Nonlinear steady-state responses of longitudinally traveling functionally graded material plates in contact with liquid, Compos. Struct. 164 (2017) 130–144.
[73] Y.Q. Wang, J.W. Zu, Vibration behaviors of functionally graded rectangular plates with porosities and moving in thermal environment, Aero. Sci. Technol. 69 (2017) 550–562.
[74] M.F. Ashby, et al., Metal foams: a design guide, Appl. Mech. Rev. 54 (2001) B105–B106.
[75] W. Lee, Cellular solids, structure and properties', Mater. Sci. Technol. 16 (2000) 233.
[76] J. Yang, D. Chen, S. Kitipornchai, Buckling and free vibration analyses of functionally graded graphene reinforced porous nanocomposite plates based on Chebyshev-Ritz method, Compos. Struct. 193 (2018) 281–294.
[77] I. Belkorissat, et al., On vibration properties of functionally graded nano-plate using a new nonlocal refined four variable model, Steel Compos. Struct. 18 (2015) 1063–1081.
[78] F. Ebrahimi, et al., Influence of Magnetic Field on the Wave Propagation Response of Functionally Graded (FG) Beam Lying on Elastic Foundation in Thermal Environment, Waves in Random and Complex Media, 2021, pp. 1–19.
[79] F. Ebrahimi, M.R. Barati, P. Haghi, Thermal effects on wave propagation characteristics of rotating strain gradient temperature-dependent functionally graded nanoscale beams, J. Therm. Stresses 40 (2017) 535–547.
[80] M. Sobhy, Buckling and free vibration of exponentially graded sandwich plates resting on elastic foundations under various boundary conditions, Compos. Struct. 99 (2013) 76–87.
[81] Y. Xue, et al., Free vibration analysis of porous plates with porosity distributions in the thickness and in-plane directions using isogeometric approach, Int. J. Mech. Sci. 152 (2019) 346–362.
[82] A. Mahi, A. Tounsi, A new hyperbolic shear deformation theory for bending and free vibration analysis of isotropic, functionally graded, sandwich and laminated composite plates, Appl. Math. Model. 39 (2015) 2489–2508.